

A Dynamical Systems and System Identification Framework for Phase–Amplitude Coupling Analysis

Rajintha Gunawardena and Fei He*

Centre for Computational Science and Mathematical Modelling, Coventry University, Coventry CV1 5FB, UK

ABSTRACT

Phase-amplitude coupling (PAC), a form of cross-frequency interaction, has been implicated in various cognitive functions and, by extension, in neural communication and information integration. Accurately detecting and characterising PAC is essential for understanding its role in processes such as memory and attention. However, this remains a significant challenge. Most existing methods rely on variations in the temporal profile to detect PAC, but they often suffer from key limitations, most notably, their sensitivity to filter bandwidth selection and their susceptibility to detecting spurious couplings. Previous studies have suggested that approaches grounded in the actual generative dynamics of PAC may offer improved accuracy. In this study, we adopt a dynamical systems perspective and propose a novel method for PAC detection and characterisation based on nonlinear system identification. This approach involves identifying a nonlinear dynamical model that captures the temporal dynamics underlying PAC. The resulting generative model enables noise-free simulation of estimated PAC signals, facilitating detailed analysis of modulation strength and the low-frequency phase at which the high-frequency bursts occur. The proposed method accounts for harmonic-induced spurious couplings through empirically derived criteria and remains robust to high noise levels and variations in slow-frequency power, offering an accurate and interpretable framework for PAC analysis. The performance of the proposed approach is illustrated using several simulated examples and a real case using local field potentials (LFP) data. The results are compared with several popular methods.

Keywords: Phase-amplitude coupling, quadratic phase coupling, nonlinear dynamics, system identification, NARX

I. INTRODUCTION

Interactions between neural oscillations, both within and across brain regions, exhibit substantial complexity, even during resting states [1–4]. As a result, understanding how spatio-temporal neural activity coordinates across multiple spatial and temporal scales has become a central question in neuroscience [5, 6]. Over the past decade, a key insight has emerged: oscillatory neural activity can engage in higher-order dynamical interactions [1, 7–11]. These interactions, occurring across distinct frequency bands, are referred to as cross-frequency coupling (CFC).

Evidence suggests that CFC arises from the dynamical interactions between large-scale neural populations and local circuits, where activity in distributed networks and local neuronal processing influence each other [5, 12–15]. As such, CFC has been proposed as a fundamental mechanism enabling communication between global and local processes, thereby facilitating large-scale information integration across the brain [16]. This hypothesis is supported by studies employing magnetoencephalography (MEG) and electroencephalogram (EEG), which have consistently identi-

fied CFC across various cognitive and sensory contexts [3, 6, 10, 13, 17, 18]. Furthermore, alterations in CFC have been associated with a range of neurological and psychiatric conditions. These include neurodegenerative diseases such as Alzheimer’s disease (AD) and Parkinson’s disease (PD) [19–24], neurodevelopmental disorders such as Attention Deficit Hyperactivity Disorder (ADHD) and autism spectrum disorder [25–27], as well as various psychiatric disorders [28–33]. These findings highlight the potential of CFC as a biomarker for pathological brain dynamics.

Amplitude–amplitude coupling, phase–phase coupling, and phase–amplitude coupling (PAC) represent distinct forms of CFC [17]. While amplitude–amplitude and phase–phase coupling have been observed, PAC has attracted particular interest within brain electrophysiology. As the most commonly observed form of CFC, functionally, PAC is directly involved in motor functions, cognitive processes, attention, sensory processing, and consciousness [9, 34–43]. Consequently, PAC analysis offers a powerful means of probing the complex cross-frequency interactions underpinning brain activity [17], thereby deepening our understanding of the neural mechanisms driving cognitive and sensory functions as well as the pathophysiology of neurological and psychiatric disorders [19, 21, 27, 30, 31, 33, 35, 40]. Conceptually, PAC refers to a cross-frequency interaction in

* Correspondence email address: fei.he@coventry.ac.uk

which the phase of a low-frequency neural oscillation is associated with, or modulates, the amplitude envelope of a higher-frequency oscillation [5, 12–15].

Metrics such as the Modulation Index (MI) [44], Mean Vector Length (MVL) [45], Generalized Linear Models (GLM) [46] and their variants [47–50] have been widely applied to detect and characterise PAC. However, accurately detecting and interpreting PAC signals remains challenging and is prone to detecting spurious PAC [51, 52]. This difficulty arises from factors such as non-sinusoidal waveforms, noise, and sharp edges or spikes in the data, all of which compromise the filtering-based analysis procedures underlying commonly used metrics [51–57]. In addition, methodological considerations such as the inappropriate selection of filter bandwidths (overly narrow or excessively broad) and analysis window lengths can lead to inaccurate measurements and spurious detections [7, 52, 53]. Therefore, continued methodological advancements remain essential to enhance the robustness and interpretability of computational techniques for detecting and characterising PAC.

PAC is believed to arise from interactions between two distinct neural populations, where the phase of slow neural oscillations from one group is linked to the amplitude or power variations in faster neural oscillations of another [6, 52, 58]. This interaction reflects a dynamic process characterised by a specific form of nonlinearity known as quadratic phase coupling (QPC) [59–64]. However, conventional PAC metrics typically overlook these underlying nonlinear dynamics, focusing instead on temporal variations in signal profiles (i.e. amplitude and phase). Consequently, it has been suggested that accurate detection of genuine cross-frequency coupling requires accounting for the nonlinear dynamics, in particular QPC, that give rise to PAC [51, 56, 65]. This highlights the need for data-driven methodologies grounded in nonlinear dynamical systems theory that explicitly model QPC in the interaction between slow and fast oscillations.

Higher-order spectral analyses, such as bicoherence and the bispectrum, which are capable of capturing QPC, have been recommended as complementary tools to the aforementioned filtering-based metrics, such as MI, MVL, and GLM, for validating genuine PAC [51, 52, 62, 64]. However, bicoherence and bispectrum alone are insufficient for reliable PAC detection, as they require high-quality, long-duration signals to achieve adequate sensitivity and specificity [64, 66, 67]. Additionally, caution must be taken to avoid spurious PAC arising from harmonics of the fundamental frequency of non-sinusoidal slow oscillations, a phenomenon known as harmonic PAC [57].

In this study, we take a fully dynamical systems perspective on PAC and employ data-driven techniques that are well-established for capturing and analysing complex nonlinear dynamics. We present a novel

methodology for detecting and characterising PAC based on nonlinear systems identification methods from control engineering, specifically the nonlinear autoregressive with exogenous input (NARX) model structure [68] combined with a Orthogonal Least Squares (OLS)-based algorithm [69], in particular the iterative Forward Regression Orthogonal Least Squares (iFRO) algorithm [70]. The use of NARX or extended NARMAX (NARX model with a moving average, MA, noise model) model structures, together with OLS-based algorithms—collectively referred to as NARMAX methods—is well established [71]. These methods have been widely applied to the study of complex systems across a wide range of disciplines [72–79]. As we demonstrate, the proposed NARX-based PAC methodology achieves high sensitivity and specificity even under high-noise conditions, performs well with short time windows, and remains robust to factors that commonly give rise to spurious PAC in conventional metrics.

The remainder of this paper is organised as follows. The section following the introduction provides an extensive review of PAC, with emphasis on the mechanisms underlying its generation and the dynamical interactions between neuronal populations. This includes an analysis of simple analytical models that can generate canonical (basic) and more complex PAC dynamics, as well as neural mass models (NMMs) that simulate the emergence of PAC in the brain. This is followed by a brief review of current methods and the problem of spurious PAC.

The subsequent methods section begins by introducing the concept of QPC, the specific nonlinear dynamics responsible for generating PAC, which serves as the conceptual basis for our proposed methodology. Afterwards, it establishes that any complex PAC can be approximately represented by its canonical form and then shows how this can be modelled using a two-input, single-output NARX model identified through nonlinear systems identification techniques. We then provide detailed procedures for implementing the NARX-based PAC methodology. The experimental results section evaluates the proposed method against commonly used PAC metrics on both synthetic and real neural data. Finally, we present a discussion, draw conclusions, and outline directions for future research.

II. PHASE-AMPLITUDE COUPLING: ANALYTICAL MODELS, CURRENT METHODS AND SPURIOUS COUPLING

Global and local processes in the brain are thought to interact through CFC, facilitating the integration of information across distributed brain regions [16]. This interaction is inherently dynamic, with oscillatory components at different frequencies influencing one another

[12, 13, 16]. Among the various forms of CFC, PAC is the most widely studied. In a PAC signal $z(t)$, the amplitude envelope (power fluctuations, $A_y(t)$) of the higher-frequency oscillation $y(t)$ is coupled to the instantaneous phase ($\varphi_x(t)$) of the lower-frequency oscillation $x(t)$ [7, 53, 57], such that $A_y(t)$ varies systematically with $\varphi_x(t)$. This is illustrated in Figure 1, which shows the decomposition of a PAC signal into its basic components: the slow (low-frequency) oscillation, $x(t)$, and the amplitude-modulated fast (high-frequency) oscillation, $y(t)$.

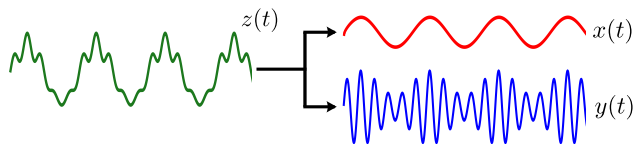


Figure 1. **Decomposition of a general PAC signal.** A PAC signal, $z(t)$, can be decomposed into two components: a low-frequency oscillation, $x(t)$, and a high-frequency oscillation, $y(t)$, whose amplitude is modulated. The amplitude envelope of $y(t)$ ($A_y(t)$) is coupled to the phase of $x(t)$ ($\varphi_x(t)$).

The PAC phenomenon has been observed in brain signals recorded using a range of methodologies, including LFP, EEG, and MEG. It has been reported across multiple brain regions, such as the auditory and prefrontal cortices [80] and the hippocampus [35, 81]. As noted earlier, PAC has been shown to play a critical role in functional neural processes, including cognitive and sensory processing [35, 37, 38, 42, 43], and has also been implicated in the pathophysiology of neurological and psychiatric disorders [27, 31, 33, 35].

Numerous studies have employed a variety of analytical approaches to model and investigate the dynamics underlying PAC. These range from relatively simple nonlinear functions [14, 62] (Fig. 2A) to more sophisticated frameworks based on coupled differential equations [1, 12, 82] (Fig. 2B). Regardless of the complexity of generating a PAC signal, it can still be decomposed into its respective slow oscillation and amplitude-modulated fast oscillation, as shown in Figure 1. It should be noted that here, an oscillation can be non-sinusoidal, contain non-stationarities, and even be broadband.

Due to methodological limitations in conventional PAC analysis procedures (further discussed in Section II C), there remains a considerable risk of detecting spurious PAC [51–53, 55–57]. As several studies have emphasised [51, 56, 65, 83], adopting methods that explicitly capture the underlying nonlinear dynamics responsible for generating PAC may offer advantages for improving detection accuracy.

This section discusses the temporal and spectral characteristics of PAC using PAC-generating dynamics,

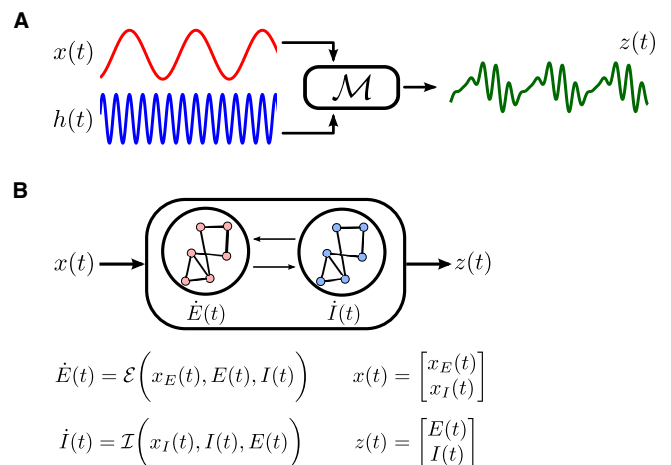


Figure 2. **Mechanisms and models for generating PAC.** **A** and **B** illustrate two model classes capable of generating PAC dynamics. **A** shows a simple analytical model of a PAC signal. In these models, a slow oscillation, $x(t)$, and a fast oscillation, $h(t)$, are combined through a nonlinear function in model \mathcal{M} to produce the PAC, $z(t)$. **B** illustrates coupled differential equations that generate PAC signals resembling those observed in neural activity. Here, the mean activity of two interacting neural populations, $E(t)$ and $I(t)$, is modelled using differential equations, $\mathcal{E}(\cdot)$ and $\mathcal{I}(\cdot)$, respectively. $x_E(t)$ and $x_I(t)$ denote the slow oscillation inputs to the neural populations E and I . The fast oscillation dynamics are generated internally due to the activity between $E(t)$ and $I(t)$. An explicit link can be established between these two types of models as described in Section II B.

ranging from simple to more complex models. It then critically reviews widely used methods, highlighting key limitations and common sources of spurious PAC detection. This motivates the use of a dynamical-systems framework for more robust PAC detection.

A. Simple analytical models of PAC

Analytical models for generating PAC are essential for understanding the complex interactions between slow and fast oscillations that give rise to this form of CFC. These models span from simple mathematical formulations to systems of ordinary differential equations (Fig. 2).

Simple PAC models (Fig. 2A) can be represented as

$$\begin{cases} z(t) = x(t) + y(t + \delta t) \\ y(t) = f\left(x(t), h(t)\right), \end{cases} \quad (1)$$

where $z(t)$ is a PAC signal; $x(t)$ is the slow oscillation; $y(t)$ is the amplitude modulation of the fast oscillation $h(t)$. $f(\cdot)$ denotes a nonlinear function that modulates

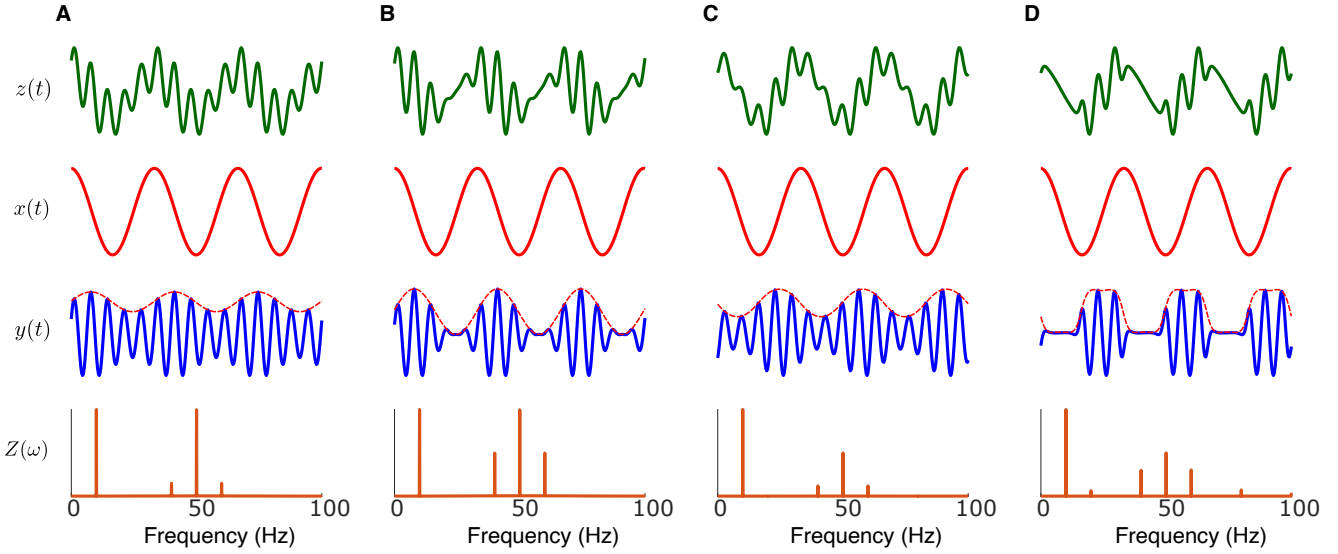


Figure 3. Effects of varying modulation parameters in illustrative PAC models. The generated PAC signals, $z(t)$, are shown in green. The 10Hz slow oscillation, $x(t)$, is shown in red, while the corresponding amplitude-modulated 50Hz fast oscillations, $y(t)$, are shown in blue, with their amplitude envelope indicated by dotted red lines. The magnitude spectrum of $z(t)$, $Z(\omega)$ is shown in orange. **A** and **B** illustrate the effect of varying the parameter m (lower vs. higher) in the basic PAC model, equations (1) and (2). Intermodulation components can be seen at 40Hz and 60Hz, with m directly controlling the modulation depth (amplitude of the red dotted envelope). Comparing **A** and **B** shows that the depth of the modulation is proportional to the magnitude of the intermodulation frequencies. **C** and **D** show the effect of varying α and c in the more complex PAC model, as given in equations (1) and (3). Due to the more complex modulation, the amplitude modulation is non-sinusoidal in **D** compared to **A** – **C**, resulting in additional intermodulation components. Parameters α and c can influence both the modulation depth (envelope amplitude in the red dotted line) and its complexity (generation of extra intermodulation components).

the amplitude of $h(t)$ according to the phase of $x(t)$. Examples of possible forms for $f(\cdot)$ include

$$y(t) = \left(1 + m \times x(t)\right)h(t). \quad (2)$$

This, along with equation (1) represents the most basic PAC model, in which the coupling strength between $x(t)$ and $h(t)$ is governed by m . While,

$$y(t) = \left(1 - \frac{1}{1 + \exp(-\alpha(x(t) - c))}\right)h(t), \quad (3)$$

is a more complex PAC model, adapted from [14]; it can generate non-sinusoidal amplitude modulations [84]. The coupling properties (including coupling strength) in equation (3) are determined jointly by the parameters α and c . The preferred phase of the coupling can be adjusted by introducing a delay of δt seconds in $y(t)$ with respect to $x(t)$ [14], as shown in equation (1). The preferred phase in PAC indicates the phase of the slow oscillation at which fast oscillatory activity tends to peak [39, 44].

The simple PAC models introduced above provide insight into the basic temporal and spectral properties

of an ideal amplitude modulation, $y(t)$, as illustrated in Figure 3. The PAC signals, $z(t)$, shown in Figure 3 and Figure 4, are generated using identical parameter settings from equations (2) and (3). However, in the case of Figure 4, a non-sinusoidal slow oscillation for $x(t)$ is used. Figures 3A-B and 4A-B are produced using the basic PAC model in equations (1) and (2), with $m = 0.5$ and $m = 1$, respectively. Figures 3C-D and 4C-D are produced using the complex PAC model—equations (1) and (3), with $\alpha = 1$ and $\alpha = 6$, respectively, and $c = 10^{-6}$ in all cases. In both Figures 3 and 4, $\delta t = 25$. The slow oscillation, $x(t)$, in Figure 3 is a 10Hz sinusoidal wave, while in Figure 4 it is a 10Hz non-sinusoidal wave generated using a Van der Pol oscillator in equation (4).

$$\frac{d^2x}{dt^2}(t) - \mu(1 - x^2)\frac{dx}{dt}(t) + x(t) = 0 \quad (4)$$

For a 10Hz non-sinusoidal wave, the oscillator in equation (4) should be simulated with $\mu = 116.5$ and the initial conditions at $t = 0$, $d^2x/dt^2 = 2$ and $dx/dt = 1$.

In general, PAC consistently generates distinct sidebands adjacent to the high-frequency component $h(t)$. This is evident in the spectrum $Z(\omega)$ in Figure 3A and B, where sidebands appear adjacent to the 50Hz com-

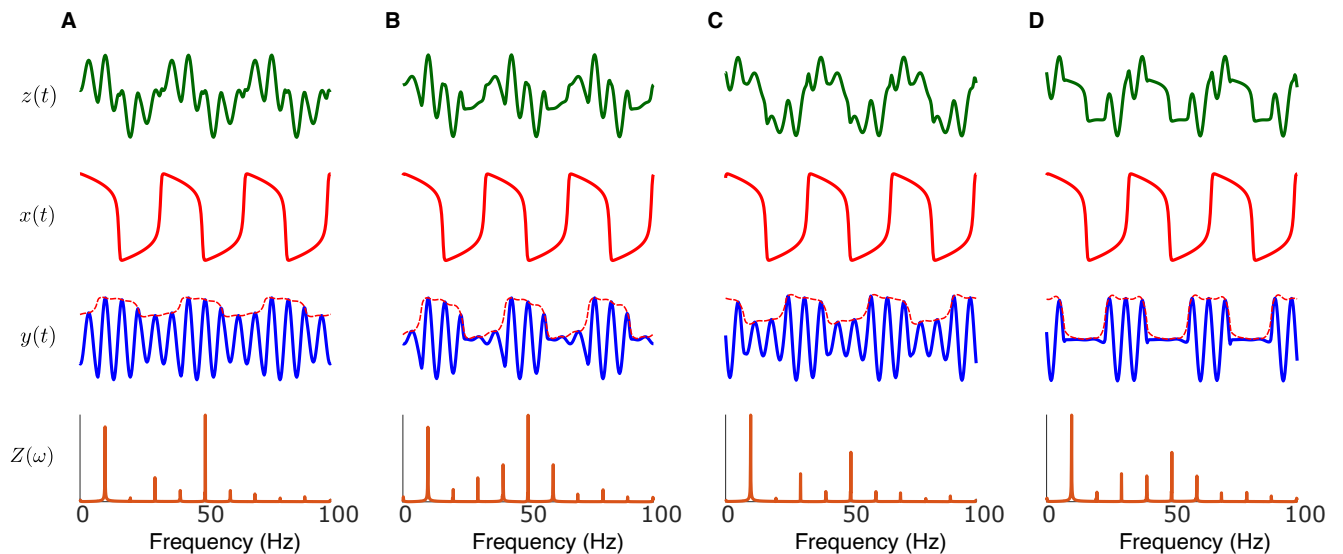


Figure 4. **Effects of non-sinusoidal input and modulation parameters in simple PAC models.** The generated PAC signals, $z(t)$, are depicted in green, while the 10Hz non-sinusoidal slow oscillation, $x(t)$, is shown in red. The corresponding amplitude-modulated 50 Hz fast oscillations, $y(t)$, with the amplitude envelope shown as dotted red lines, are depicted in blue. The magnitude spectrum of $z(t)$, $Z(\omega)$ is shown in orange. This figure is generated with the same corresponding modulation parameters as in Figure 3, but with a non-sinusoidal slow oscillation. **A** and **B** show the variation of m in the basic PAC model, equations (1) and (2). In comparison to Figure 3A and Figure 3B, the additional frequencies are because of the harmonics in the non-sinusoidal slow oscillation and because of this, extra intermodulations are produced by the resulting non-sinusoidal amplitude modulation (see envelope of $y(t)$ in **A** and **B**). The contribution of the extra intermodulations is more apparent in **B** as the modulation depth (envelope of $y(t)$) is directly proportional to the magnitudes of all the intermodulations. **C** and **D** show the variations of α and c in the more complex PAC model shown in equations (1) and (3).

ponent. These sidebands result from the amplitude of the high-frequency oscillation varying in synchrony with the phase of the low-frequency oscillation, $x(t)$, as illustrated in Figure 3A and B. Such sidebands are also referred to as intermodulations. Later in Section III A, intermodulations are discussed in the context of nonlinear dynamics.

Altering the coupling parameters in the simple PAC models changes the amplitude modulation depth [44], with stronger phase–amplitude coupling corresponding to a greater modulation depth. This is evident from the increased envelope amplitude of $y(t)$ (dotted red line) when comparing Figure 3A to Figure 3B and Figure 3C to Figure 3D. In the spectral domain, this change manifests as an increase in the magnitude of the sidebands relative to the magnitude of the high-frequency component (in Fig. 3, compare $Z(\omega)$ in A to B and in C to D). Non-sinusoidal amplitude modulations (i.e. the envelope of $y(t)$ is non-sinusoidal) can be generated by varying α in equation (3) from 1 to 6 (in Fig. 3, C to D). Such non-sinusoidal modulation introduces additional sidebands in the spectrum, as observed in $Z(\omega)$ in Figure 3D.

In real brain electrophysiology, slow oscillations are often non-sinusoidal in nature [21, 85]. Consequently,

when the slow oscillation, $x(t)$, is non-sinusoidal, the spectrum of the PAC signal ($Z(\omega)$ in Figure 4A and B) contains many more frequency components than that of a purely sinusoidal PAC signal ($Z(\omega)$ in Figure 3A and B). These additional components arise from two sources: (1) harmonics due to the inherent non-sinusoidal nature of the slow oscillation $x(t)$, and (2) the non-sinusoidal amplitude modulation of $y(t)$ (similar to the case shown in Fig. 3D). The latter effect is particularly evident when comparing $Z(\omega)$ in Figure 4A and B, where m increases from 0.5 to 1 (equation (2)) and in Figure 4C and D, where α increases from 1 to 6 (equation (3)). These extra frequency components can contribute to the detection of spurious PAC, as discussed later in this section.

The sidebands adjacent to the high-frequency component are known as immediate sidebands. A direct comparison of Figures 3 and 4 shows that changes in modulation depth are directly reflected in the relative magnitude of the immediate sidebands to the magnitude of the high-frequency component. In essence, for PAC, the modulation depth is proportional to the ratio between the magnitudes of the immediate sidebands and the high-frequency component.

PAC can be broadly classified into two types:

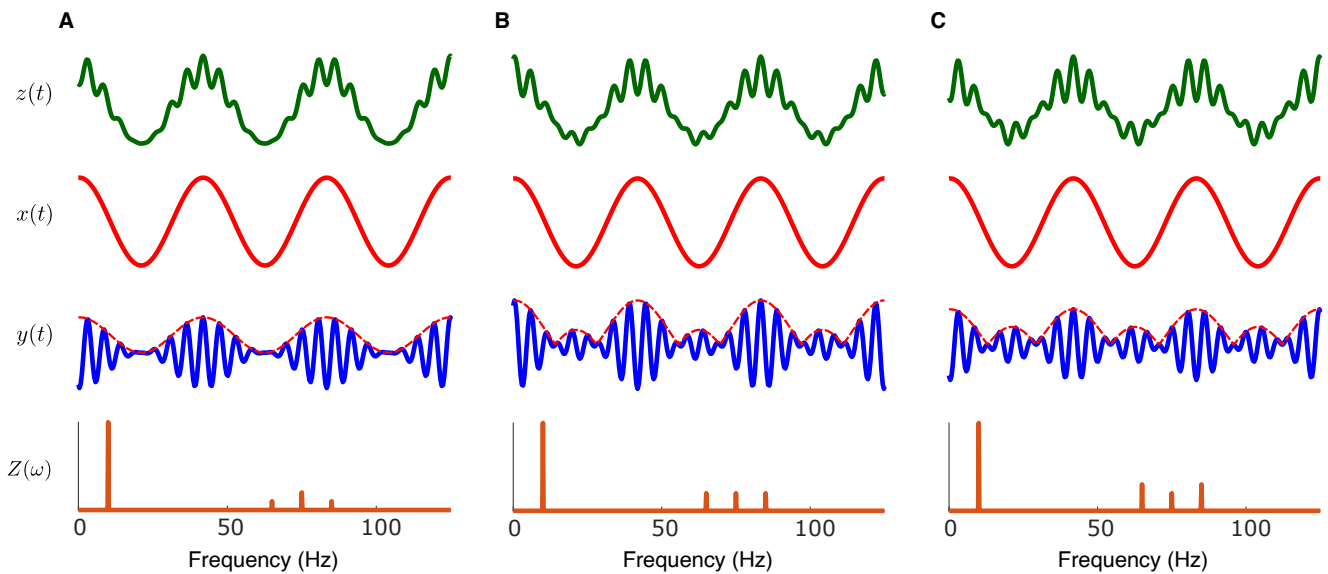


Figure 5. **Monophasic and biphasic PAC.** This figure illustrates the transition from monophasic (**A**) to biphasic (**B** and **C**) PAC using the basic PAC model, equations (1) and (2). The generated PAC signals, $z(t)$, are depicted in green, while the 10Hz sinusoidal slow oscillation, $x(t)$, is shown in red. The corresponding amplitude-modulated 75Hz fast oscillations, $y(t)$, with the amplitude envelope shown in dotted red lines, are depicted in blue. The magnitude spectrum of $z(t)$, $Z(\omega)$ is shown in orange. The modulation parameter, m , in equation (2) is increased from its level in **A** to transition from monophasic to biphasic PAC in **B**. After this point, a further increase in m increases the depth of modulation at the second phase. This is shown in **C**.

monophasic and biphasic [44]. The discussion thus far has focused on monophasic PAC. Both forms can be generated using the basic PAC model (i.e. equations (1) and (2)), as illustrated in Figure 5. In this example, $x(t)$ is a 10Hz sinusoid, $h(t)$ is a 75Hz sinusoid with an amplitude of 0.2, and $\delta t = 0$. The coupling parameter m in equation (2) is varied across [1, 2, 3] in Figures 5A, B, and C. In monophasic PAC, the amplitude of the high-frequency oscillation is modulated by a single phase of the low-frequency oscillation, $x(t)$ (i.e. $y(t)$ in Fig. 5A). This typically manifests as an amplitude increase in $y(t)$ at a specific phase of the low-frequency cycle, with lower amplitude over the remainder of the cycle, reflecting a simple and consistent coupling between the two oscillations. In contrast, biphasic PAC occurs when the amplitude of the high-frequency oscillation is modulated by two distinct phases of the low-frequency oscillation, separated by 180 degrees (π radians), for instance, at both the peak and trough of $x(t)$ (see $y(t)$ in Fig. 5B). This produces two bursts of high-frequency activity within a single low-frequency cycle. In the frequency spectrum, biphasic PAC is characterised by sidebands (intermodulations) whose magnitudes can approach or exceed that of the high-frequency component (see $z(t)$ in Fig. 5 B and C).

While the models discussed above provide insight into the basic mechanisms underlying PAC generation, they do not capture the emergence of PAC arising from dy-

namic interactions between distinct neural populations. To capture these interactions, a neural mass model (NMM) can be more suitable, as it describes the collective dynamics of neuronal populations through differential equations [82].

B. Neural mass models for generating PAC

A NMM represents neuronal populations as continuous entities, simulating their collective dynamics. These models can incorporate substantial biological detail, including excitatory and inhibitory neuron types, synaptic delays, and neurotransmitter effects [1, 86]. As such, NMMs provide a powerful framework for investigating the emergence of PAC from the interactions within and between neural populations [12, 87, 88].

One of the most fundamental examples of a NMM is the Wilson-Cowan model [89, 90], which describes the average activity of excitatory, inhibitory and pyramidal neural populations through coupled differential equations [91]. Extending this framework, NMMs can be combined to form a complex network of neural populations, providing a more realistic representation of cortical column activity [92]. Here, we employ a simplified NMM capable of generating PAC [82] (equations (5)-(7)) to illustrate how complex PAC signals can emerge from the dynamic interaction between neural popula-

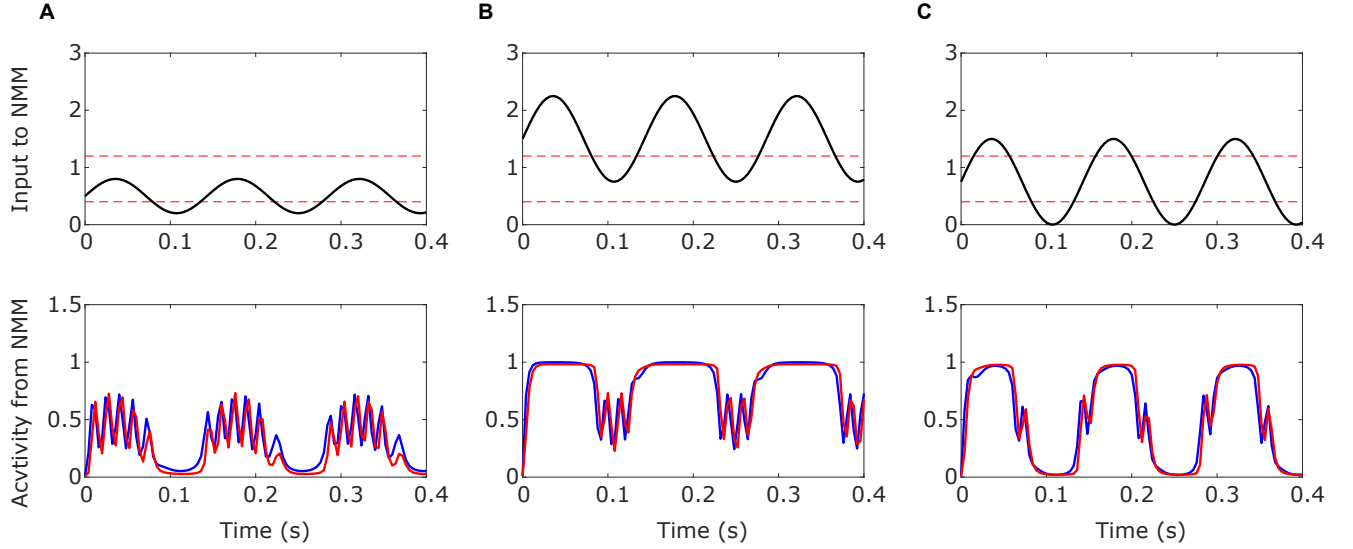


Figure 6. **Different forms of PAC induced by a 7Hz theta input to the excitatory population of a NMM.** The following parameters were used for equations (5)-(7) as given in [82]; $\tau_E = \tau_I = 0.0032$, $w_{EE} = 2.4$, $w_{IE} = w_{EI} = 2$, $b = 4$. The inhibitory input was set to $x_I(t) = 0$. The low-frequency input to the excitatory population, $x_E(t)$ in equation (5), was a 7 Hz theta sinusoid (black curve), $x_E(t) = A_E \cos(2\pi \times 7 \times t) + \bar{x}_E$, where A_E and \bar{x}_E were varied to produce the PAC activity shown. The red and blue curves represent neural activity from the inhibitory (I) and excitatory (E) populations, respectively. This particular NMM produces intrinsic gamma activity when $0.4 \leq x_E(t) \leq 1.2$ (red dotted lines on the top panels). **A.** $A_E = 0.3$ and $\bar{x}_E = 0.5$. Gamma oscillations align with the peak phase of the theta input, consistent with PAC in which high-frequency activity is nested within the crest of the slower oscillation. **B.** $A_E = 0.75$ and $\bar{x}_E = 1.5$. The high-frequency gamma oscillations burst around the trough of the theta input, opposite to case **A**. Here, the timing of gamma oscillations shifts from the peak to the trough of the theta wave. **C.** $A_E = 0.75$ and $\bar{x}_E = 0.75$. Gamma oscillations synchronise with both the rising and falling phases of the theta input, yielding a more complex PAC pattern. This occurs when $x_E(t)$ crosses the interval $0.4 \leq x_E(t) \leq 1.2$ at two points within each theta cycle.

tions. This NMM model represents the average activity of an excitatory group of neurons, E , as given in equation (5), and an inhibitory group of neurons, I , as given in equation (6).

$$\tau_E \dot{E}(t) = -E(t) + f(x_E(t) + w_{EE}E(t) - w_{IE}I(t)), \quad (5)$$

$$\tau_I \dot{I}(t) = -I(t) + f(x_I(t) + w_{EI}E(t)). \quad (6)$$

In both equations (5) and (6), a sigmoid function,

$$f(z) = \frac{1}{1 + e^{-b(z-1)}}, \quad (7)$$

is used as an activation function for both E and I neural populations.

As described in [82], these populations are reciprocally connected, i.e. $w_{IE}I(t)$ in equation (5) and $w_{EI}E(t)$ in equation (6). Thus, the excitatory and inhibitory populations can mutually drive one another, while the inhibitory population can also suppress the activity of the excitatory population. External inputs to both E and I populations are included as $x_E(t)$ in equation (5) and $x_I(t)$ in equation (6). The reciprocal connections between them and a self-feedback mechanism

for the excitatory population ($w_{EE}E(t)$ in equation (5)) are crucial for the model to generate intrinsic oscillations. Together, these mechanisms enable the model to produce high-frequency gamma waves nested within low-frequency theta rhythms (i.e. a PAC). By varying the amplitude and the mean of the low-frequency theta input ($x_E(t)$ or $x_I(t)$ in equation (5) or (6)), the model can alter the phase relationship of the coupling and switch between monophasic and biphasic PAC [82]. This behaviour is illustrated in Figure 6. Further details on this NMM model and its parameterisation are provided in [82].

The ability of the Wilson-Cowan model to generate PAC through simple adjustments to connection strengths and external inputs suggests a fundamental mechanism that may explain its widespread presence in the brain. Furthermore, the model's flexibility in producing oscillations locked to various phases of an input signal is consistent with empirical observations [9, 93] and highlights its potential to inform both experimental and theoretical investigations into the neural underpinnings of cognitive processes [82].

An explicit link can be established between the NMM defined by equations (5)–(7) and the simple analytical

PAC model in (1) (Section II A). This is achieved by applying a Taylor expansion to the shifted and scaled sigmoid function $f(z)$ in (7), as detailed in Appendix B 2. As shown there, the NMM output (e.g. $E(t)$) can be interpreted as an internally generated fast oscillation, $h(t) = w_{EE}E(t) - w_{IE}I(t)$, whose amplitude is modulated by the slow input $x_E(t)$. Moreover, the NMM output can be decomposed into a slow component, $x(t)$, and an amplitude-modulated fast component, $y(t)$, consistent with the representation in Figure 1.

C. Common metrics used for measuring PAC

Numerous techniques have been proposed to identify PAC, each with distinct strengths and limitations. Most quantify the relationship between the phase of a low-frequency oscillation and the amplitude envelope of a higher-frequency oscillation. The most widely used (standard) approaches first apply bandpass filtering to isolate the low- and high-frequency oscillations. They then estimate the low-frequency phase and the high-frequency amplitude envelope [44, 94] (Fig. 7). Although these methods share the goal of measuring PAC, differences in their conceptual bases and mathematical formulations lead to varying sensitivity and suitability across datasets and experimental conditions. Several reviews summarise and compare these approaches [44, 58, 95], with Tort *et al.* [44] providing a particularly comprehensive assessment of commonly used PAC metrics. Among these methods, the MI, Phase-Locking Value (PLV), and MVL remain the most widely employed [94]. Hulsemann *et al.* [94] extended earlier evaluations under more realistic settings (e.g. noise and non-ideal PAC) and also considered the Generalized Linear Modelling Cross-Frequency Coupling (GLM-CFC) metric.

Hulsemann *et al.* [94] found that PLV, MVL, MI, and GLM-CFC can distinguish PAC strength and width under monophasic coupling, but only MI and GLM-CFC reliably detect biphasic coupling. All four metrics are sensitive to data length, signal-to-noise ratio (SNR), and sampling rate. Under noise, MI and GLM-CFC are the most robust to changes in coupling strength, whereas MVL is most sensitive in high-SNR settings. Overall, MI is consistently the most robust across common confounds [44, 94], while PLV is comparatively less reliable. As emphasised in multiple studies [7, 58, 94], no single definitive standard for measuring PAC currently exists. The choice of metric should therefore be guided by the experimental goals and data characteristics, with a combined use of complementary PAC measures generally recommended.

It is also crucial to note that these techniques can sometimes falsely suggest the presence of PAC, even in the absence of genuine dynamic interactions between

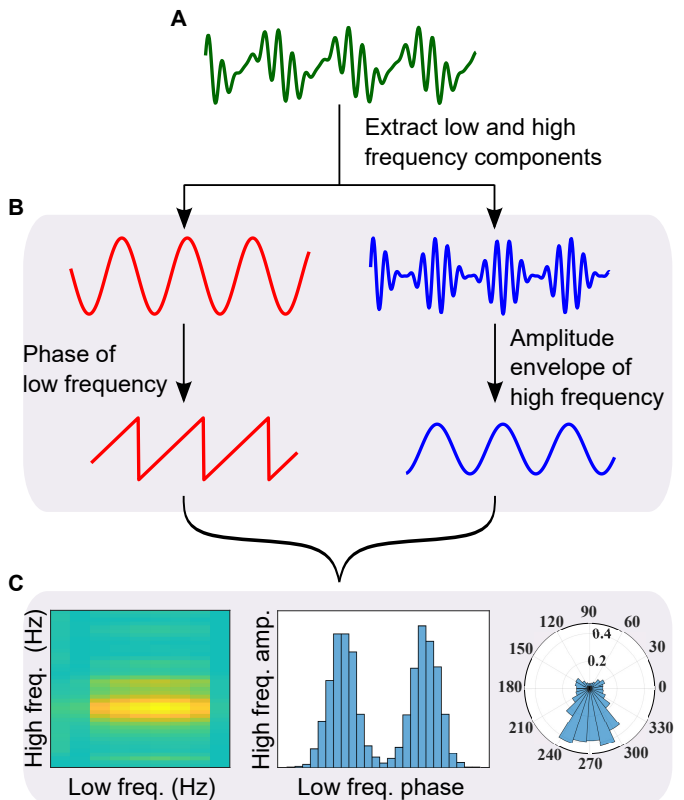


Figure 7. **General procedures in standard methods for detecting PAC.** The PAC signal (A) is decomposed or bandpass-filtered to obtain the low-frequency and high-frequency oscillations (B). As shown in B, the phase of the low-frequency oscillation is estimated, and the amplitude envelope of the high-frequency oscillation is extracted. Depending on the metric used, one then assesses whether the variation of the amplitude envelope is synchronised with the phase of the low-frequency oscillation. Regardless of the metric used, this information is usually visualised in a comodulogram (first panel in C). The second panel in C shows how the fast oscillation’s amplitude varies with the slow oscillation’s phase, as used in the MI metric [44]. The third panel illustrates the vector representation used for the MVL metric [45], where each vector’s angle is given by the slow oscillation phase, and its length is the corresponding fast oscillation amplitude at a certain time instance.

neural oscillations, thereby leading to the detection of spurious PAC. This issue has been explored in detail by [51, 52], highlighting the importance of methodological refinement. Consequently, the study of PAC remains an evolving field in which continuous methodological advancements and conceptual developments are essential to enhance the accuracy and interpretability of current and future computational approaches.

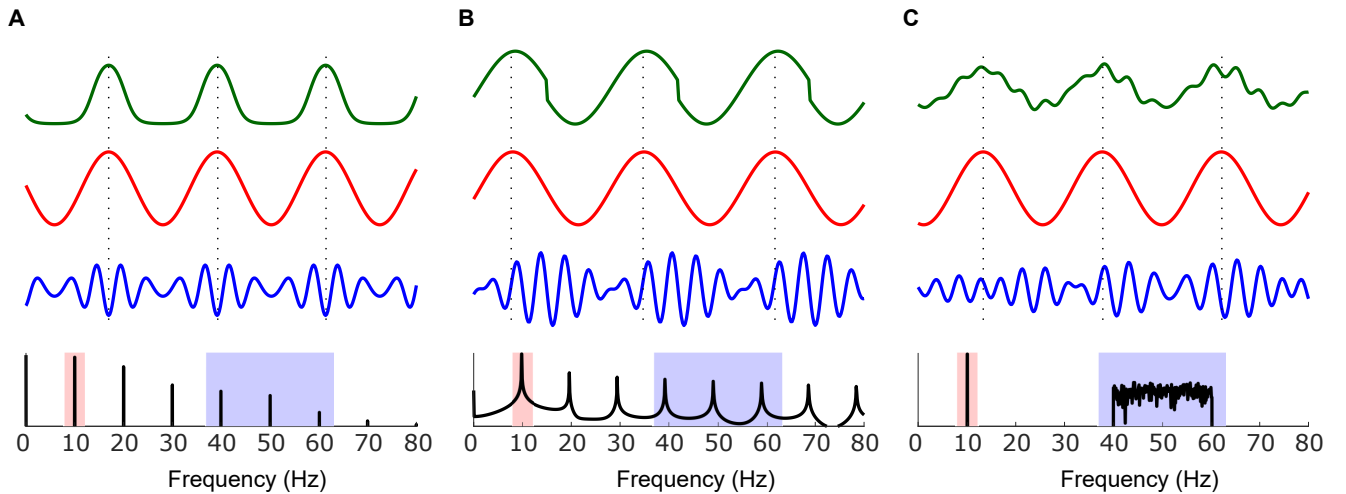


Figure 8. **Signals that can lead to spurious detection of PAC in neural recordings.** The three types of signals that may produce spurious PAC are shown in green, and the corresponding spectrum is shown in black. The bandpass-filtered low-frequency component is shown in red (with the corresponding passband indicated by the red shaded region). Similarly, the corresponding high-frequency component is depicted in blue (with its passband indicated by the blue shaded region in the spectrum). **A** and **B** show non-sinusoidal waveforms whose harmonics can be misinterpreted as cross-frequency coupling. **C** is a sinusoidal signal with noise that may show an apparent phase-locking between the high-frequency activity and the low-frequency signal within certain time windows. Such signal characteristics (green) are known to give rise to spurious detection of PAC.

D. Spurious PAC

Limitations in standard PAC detection procedures (Fig. 7) are a major source of spurious PAC [7, 51, 52]. While designed to assess the interaction between low- and high-frequency activity, these methods are prone to false positives when signals contain sharp edges or non-sinusoidal waveforms [51], i.e. phase-locked harmonics at integer multiples of the base frequency [55, 57] (Fig. 8). When processed with standard PAC methods, these harmonics can be mistaken for true coupling, leading to spurious PAC [51, 52, 55, 57]. Similar artefactual effects may arise from spike-related neural activity (periodic spiking) [53, 54].

Filter bandwidths and analysis window lengths are also critical considerations [52]. Wider high-frequency filter bands can overlap sub-bands that reflect distinct processes and phase relationships [93], while overly narrow low-frequency filter bands can distort non-sinusoidal rhythms [85, 96] and bias phase estimation. Likewise, shorter time windows risk inflating PAC due to noise, whereas longer windows may introduce non-stationarities.

To mitigate these challenges, it is essential to adapt standard PAC algorithms carefully and to inspect unfiltered data closely [51–53, 57]. Recommended practices include visual inspection of amplitude envelopes, event-related averaging, power spectral analysis, and bicoherence analysis [51, 53, 57]. Equally important are the

selection of appropriate filter parameters, adherence to established methodological guidelines, and optimisation of analysis window lengths to minimise the risk of spurious PAC [52]. Ultimately, methodological rigour is vital when applying standard PAC estimation techniques.

Genuine PAC arises from the dynamic interaction of neuronal populations, in which the phase of a slow oscillation in one group modulates the amplitude envelope of a fast oscillation in another. Standard PAC procedures (as described in Section II C), however, are generally not designed to capture these underlying dynamics. Verifying true PAC across frequencies, therefore, requires accounting for the complex nonlinear interactions between slow and fast oscillations [51, 56, 65]. This challenge motivates the development of data-driven methodologies capable of characterising such nonlinear mechanisms, i.e. a nonlinear systems approach. The following section explores this perspective in detail.

III. PROPOSED METHOD

This section outlines the proposed approach, which applies system identification to characterise PAC. We begin by introducing a nonlinear-systems perspective on quantifying PAC. We then show that any PAC signal generated by complex dynamics can be transformed into a canonical form that can be expressed as a nonlinear dynamical system. This canonical form can subse-

quently be estimated using nonlinear system identification, a process we refer to as canonical approximation.

A. A nonlinear systems perspective on PAC

In linear systems, the output preserves the frequency composition of the input. In contrast, nonlinear systems generate outputs with an expanded spectrum, containing frequency components beyond those present in the input signal [97–99]. For example, if the input contains a single frequency ω_1 , the output may include not only ω_1 but also its harmonics (e.g. $2\omega_1$ and $3\omega_1$). With multiple input frequencies (e.g. $\omega_1, \omega_2, \omega_3$), the output can contain the original input frequencies, their harmonics, and additional intermodulation terms, such as $\omega_1 - \omega_2$, $\omega_1 - \omega_2 + \omega_3$, or $\omega_1 + \omega_3$ [97–99]. In the nervous system, harmonic interactions, where outputs are integer multiples of inputs (e.g. $\omega_1 \rightarrow 2\omega_1$), are associated with resonant properties of neural processing circuits [85, 100–102]. Intermodulation effects, where multiple inputs combine to produce new frequencies (e.g. $\{\omega_1, \omega_2\} \rightarrow \omega_1 + \omega_2$), are associated with functional integration across neural circuits [103–106].

Harmonics and intermodulations arise from different orders of nonlinearity [97, 98], i.e. second, third, fourth, and higher, whereas first-order corresponds to linearity. An n^{th} -order nonlinearity ($n \geq 2$) specifies how many input frequency components are combined (or interact) within that order to produce new output frequencies, giving rise to both harmonics and intermodulation terms [97, 98]. For example, consider an input containing two discrete frequencies, $\{\omega_1, \omega_2\}$. A third-order nonlinearity generates only frequency components of the form $\sum_{i=1}^3 \pm \bar{\omega}_i$, where $\bar{\omega}_i \in \{\omega_1, \omega_2\}$ (typically restricting to positive frequencies). Consequently, the third-order response includes the original input frequencies $\{\omega_1, \omega_2\}$, the third-order harmonics $\{3\omega_1, 3\omega_2\}$, and several intermodulation frequencies, such as $\omega_1 + \omega_1 + \omega_2$ and $\omega_2 + \omega_2 - \omega_1$.

In the framework of nonlinear dynamics, PAC arises from second-order (quadratic) frequency coupling [59–62, 64]. This can be illustrated by examining the output spectrum of the most basic PAC model (equations (1) and (2), Section II A). Let the slow oscillation be $x(t) = \cos(\omega_S t + \phi_S)$ and the fast oscillation $h(t) = \cos(\omega_F t + \phi_F)$. Substituting these into equation (2), the simplest form of amplitude modulation is $y(t) = [1 + m \cos(\omega_S t + \phi_S)] \cos(\omega_F t + \phi_F)$ [62, 64], which can be further expanded using double-angle iden-

ties to obtain

$$y(t) = \frac{m}{2} \cos\left((\omega_F - \omega_S)t + (\phi_F - \phi_S)\right) + \cos(\omega_F t + \phi_F) + \frac{m}{2} \cos\left((\omega_F + \omega_S)t + (\phi_F + \phi_S)\right). \quad (8)$$

In equation (2), the nonlinear effects arise from the product $x(t) \times h(t)$. As shown in equation (8), this interaction generates second-order intermodulation terms between the slow and fast frequencies ω_S and ω_F ($\omega_F \pm \omega_S$). Thus, the dynamic interplay between slow and fast oscillations across neuronal populations that underlies PAC can be understood as a second-order intermodulation effect [62, 64].

In equation (8), let $t = t + \delta t$ to obtain a time-shifted amplitude modulation signal $y(t + \delta t)$. Substituting this expression into equation (1) yields a more general basic PAC signal:

$$z(t) = \cos(\omega_S t + \phi_S) + \frac{m}{2} \cos\left(\omega_\Delta t + (\phi_\Delta + \omega_\Delta \delta t)\right) + \cos\left(\omega_F t + (\phi_F + \omega_F \delta t)\right) + \frac{m}{2} \cos\left(\omega_\Sigma t + (\phi_\Sigma + \omega_\Sigma \delta t)\right), \quad (9)$$

where $\omega_\Delta = \omega_F - \omega_S$, $\phi_\Delta = \phi_F - \phi_S$, $\omega_\Sigma = \omega_F + \omega_S$, and $\phi_\Sigma = \phi_F + \phi_S$.

From equation (9), it is clear that the slow and fast oscillations (ω_S and ω_F) maintain a specific phase relationship with their intermodulation frequencies (ω_Δ and ω_Σ). This second-order intermodulation forms the basis of PAC and is referred to as a quadratic phase coupling (QPC) [59–64]. More generally, when two frequencies generate a third frequency through a second-order nonlinearity, all three frequencies are quadratically phase-coupled (either as a second-order harmonic or as a second-order intermodulation). Formally, QPC between ω_1 , ω_2 , and $\omega_3 = |\omega_1 \pm \omega_2|$ is defined as

$$|\Delta\varphi| = |\varphi(\omega_1) + \varphi(\omega_2) - \varphi(\omega_3)| = C, \quad (10)$$

where $\varphi(\omega_i)$ denotes the phase of frequency ω_i , and C is a constant. If $|\Delta\varphi|$ remains constant, ω_1 and ω_2 are said to be quadratically phase coupled with ω_3 . In the case of equation (9), $|\Delta\varphi| = \omega_S \delta t$. If the phases of the frequency components in $z(t)$ (equation (9)) are independent and random, meaning $|\Delta\varphi|$ is not constant, then $z(t)$ reduces to a simple superposition of signals at those frequencies, without coupling. Accurately characterising this dynamic property of PAC enables robust detection and quantification without the need to rely on phase estimation methods, such as the Hilbert transform, for detecting PAC.

Equation (9) shows that the minimal spectral signature of PAC consists of a low-frequency component ω_S ,

a high-frequency component ω_F , and the two symmetric second-order intermodulation components at $\omega_F \pm \omega_S$. Importantly, these four components are quadratic phase coupled (equation (10)). As outlined in the next section, this motivates a canonical PAC representation: keeping exactly the components required for second-order intermodulation, while treating additional harmonics or higher-order intermodulations as waveform details rather than the defining mechanism. This is discussed in the next section.

B. Canonical form of PAC signals

Realistic PAC signals often contain frequency components beyond the most basic form of PAC (equation (9)). For example, non-sinusoidal slow oscillations introduce harmonics, and stronger or more complex nonlinearities can create higher-order intermodulations (e.g. Fig. 3D and Fig. 4). These extra frequency components can be important for the resulting waveform and spectrum, but as discussed in this section, they are not required to establish PAC in principle. Thus, it is useful to reduce any PAC signal to its simplest (canonical) form, similar to equation (9).

PAC can be generated through different mechanisms. In the simple analytical models (Section II A), a slow oscillation $x(t)$ explicitly modulates a fast oscillation $h(t)$ through a nonlinear operation (e.g. equations (2) and (3)). Conversely, in NMMs (Section II B), the amplitude-modulated fast oscillation emerges from the internal dynamics of the excitatory–inhibitory interactions (equations (5) and (6)). These mechanisms differ considerably, however, as discussed here, the observable PAC signal still exhibits the same defining dynamical property established in Section III A: PAC, in its basic form, is determined by the QPC relationship between the slow and fast oscillation frequencies ω_S and ω_F and their second-order intermodulations ($\omega_F \pm \omega_S$).

In the PAC model given by equations (1) and (3), the nonlinear operation is more elaborate than the basic PAC model (equations (1) and (2)), often producing a non-sinusoidal amplitude modulation (Fig. 3D). In addition to the dominant second-order intermodulations, higher-order intermodulation frequencies may also appear. However, as shown in Appendix B 1, a first-order Taylor approximation of this more complex PAC model (equation (B4)) reduces to a form similar to the basic PAC model containing the key nonlinear term, $x(t) \times h(t)$, responsible for producing two second-order intermodulations. Likewise, for the biophysically derived NMM, as shown in Appendix B 2, a second-order Taylor approximation yields an analogous structure to the basic PAC model in which the slow oscillation input to the NMM modulates the amplitude of a fast oscillation generated by the internal dynamics. There-

fore, to first approximation, and from the perspective of the resulting spectral mixing, PAC-generating mechanisms can be represented as an effective two-input, single-output nonlinear system, where interaction between a slow oscillation and a fast oscillation gives rise to second-order intermodulations.

In light of the above, any PAC signal can, in its simplest approximation, be expressed as the sum of four sinusoids (equation (9)) with the frequencies: $\{\omega_S, \omega_F, \omega_F + \omega_S, \omega_F - \omega_S\}$. Their relative phases specify QPC. The depth of amplitude modulation or the coupling strength is indicated by the ratio of the magnitudes of the intermodulation components ($\omega_F \pm \omega_S$) to the fast oscillation frequency ω_F . We refer to this as the *canonical form of PAC*, which serves as the foundation for the detection and characterisation framework developed in this study.

The canonical form defines a concrete target for model-based PAC detection: given a slow oscillation and a fast oscillation with corresponding frequencies ω_S and ω_F , a second-order dynamical model is identified to capture the interaction that produces the canonical form of PAC and to encode QPC between $\{\omega_S, \omega_F\}$ and their intermodulations $\omega_F \pm \omega_S$. This is illustrated in Figure 9.

C. Canonical approximation of PAC using system identification

In this study, we propose using a control-systems analysis tool, specifically nonlinear system identification, to detect and characterise PAC. System identification constructs data-driven input–output models of dynamic processes [107]; within this framework, as shown below, polynomial NARX models [68] are well suited to the task because they predict future outputs from linear and nonlinear combinations of past inputs and outputs. Polynomial NARX identification has been widely applied to complex systems [72–79]. Here, it is used to identify spectral components that arise as second-order intermodulation products and to decompose the resulting model into linear and nonlinear parts, thereby separating slow-oscillation dynamics from amplitude-modulated fast-oscillation dynamics. A brief overview of system identification of a two-input, single-output polynomial NARX structure is provided in Appendix A. As detailed in Appendix A 2, the open-source MATLAB toolbox *NonSysID* [108, 109] is used to implement polynomial NARX model identification.

Here, we present analytically how the canonical approximation of any PAC signal naturally arises from a second-order input-only NARX model. Essentially, QPC between two frequencies is captured by identifying NARX models using *only past input values*. Let $u_1(t) = \cos(\omega_S t)$ and $u_2(t) = \cos(\omega_F t)$, where $\omega_S <$

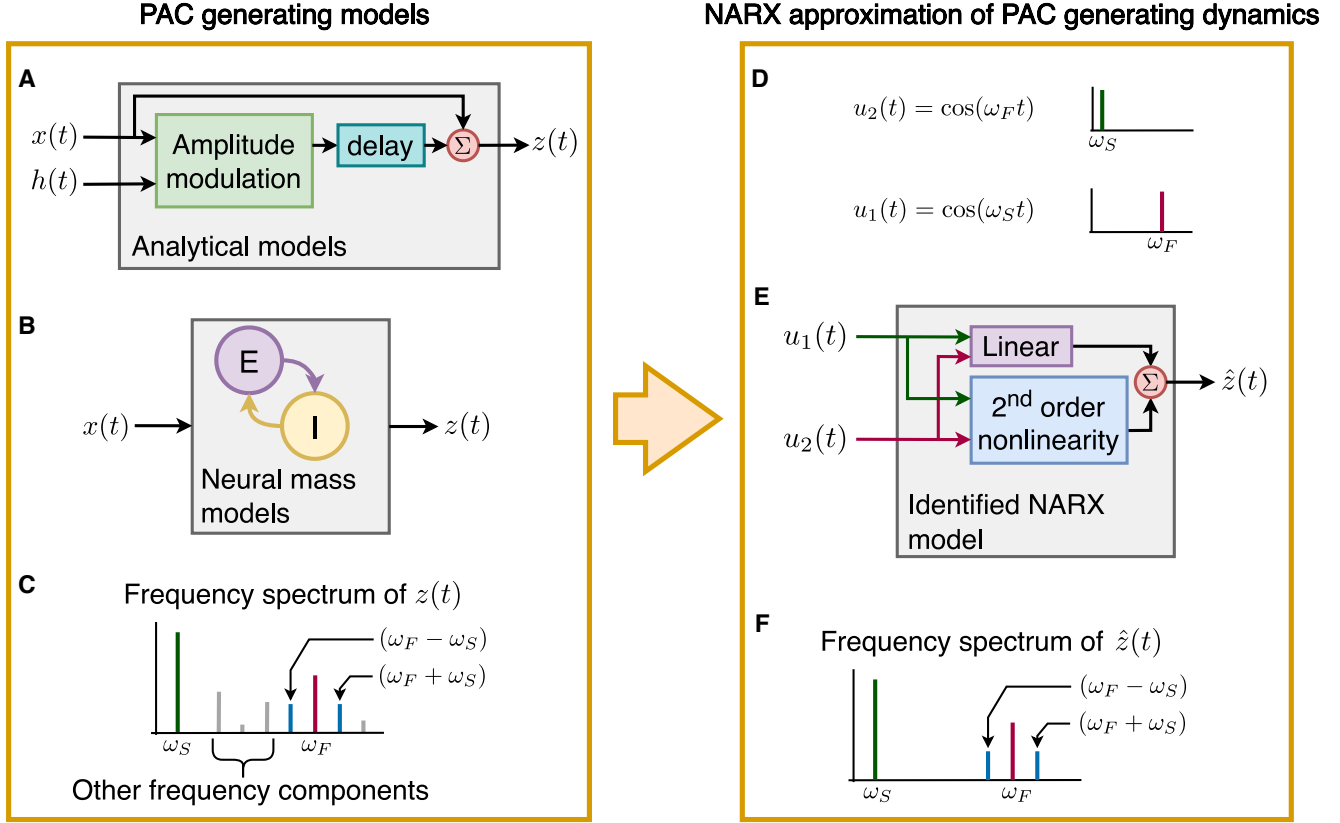


Figure 9. **A two-input single-output NARX model can be used to approximate PAC-generating dynamics.** In simple PAC models, depicted in **A**, a nonlinear operation (equations (2) and (3)) between a low-frequency oscillation, $x(t)$ and a high-frequency oscillation, $h(t)$, oscillation produces a PAC signal $z(t)$. NMMs, depicted in **B**, produce PAC signals more representative of neural activity. A NMM generates PAC signals, $z(t)$, according to the low-frequency oscillation, $x(t)$, it receives, while the high-frequency dynamics are generated within the NMM (see Section II B). **C** illustrates the typical spectrum of $z(t)$ generated by models such as in **A** and **B**. As seen from **C**, non-sinusoidal slow oscillations (Fig. 4) and non-sinusoidal PAC (Fig. 3D) can introduce additional frequency components. However, two sinusoidal inputs, as depicted in **D**, when subjected to a second-order nonlinearity, can in general approximate any PAC dynamics (i.e. QPC as described in Section III A). As proposed in this study, system identification can be used to learn a two-input single-output NARX model (as shown in **E**), to capture PAC dynamics (or QPC). The spectral profile of the identified NARX model, **F**, will provide a canonical approximation of the spectral profile of an actual PAC signal, such as in **C**.

ω_F . Introducing arbitrary time delays κ and λ , we have $u_1(t - \kappa) = \cos(\omega_S t - \omega_S \kappa)$ and $u_2(t - \lambda) = \cos(\omega_F t - \omega_F \lambda)$. The product $u_1(t - \kappa) \times u_2(t - \lambda)$, when expanded via the double-angle trigonometric identities, yields two sinusoidal components with frequencies $\omega_\Delta = \omega_F - \omega_S$ and $\omega_\Sigma = \omega_F + \omega_S$, with their respective phase angles determined by the phases of $u_1(t - \kappa)$ and $u_2(t - \lambda)$.

It is a well-established result that the sum of two sinusoids of identical frequency produces a single sinusoid of the same frequency, with amplitude and phase determined by the original components [110] (also called the phasor addition rule). Accordingly, by employing appropriate combinations of delayed terms, the following

decompositions hold:

$$A_1 \cos(\omega_S t + \phi_1) = \sum_i a_1^i \times u_1(t - \kappa_i) \quad (11)$$

$$A_2 \cos(\omega_F t + \phi_2) = \sum_j a_2^j \times u_2(t - \lambda_j) \quad (12)$$

$$\frac{A_3}{2} \left(\cos(\omega_\Delta t + \phi_\Delta) + \cos(\omega_\Sigma t + \phi_\Sigma) \right) = \sum_{i,j} a_3^{i,j} \times u_1(t - \kappa_i) u_2(t - \lambda_j), \quad (13)$$

where a_1^i , a_2^j and $a_3^{i,j}$ (for the respective i and j) are real-valued constants. Therefore, in analogy with equation

(9), the basic PAC signal can be represented as

$$z(t) = \sum_i a_1^i u_1(t - \kappa_i) + \sum_j a_2^j u_2(t - \lambda_j) + \sum_{i,j} a_3^{i,j} u_1(t - \kappa_i) u_2(t - \lambda_j). \quad (14)$$

The representation in equation (14) can be modelled via a two-input (i.e. $u_1(t) = \cos(\omega_S t)$ and $u_2(t) = \cos(\omega_F t)$), single-output, 2nd-order input-only NARX model. As indicated in equations (11)–(13), the magnitudes and phases of the constituent frequency components in $z(t)$ can be determined by selecting appropriate delay terms and coefficients, namely $a_1^i u_1(t - \kappa_i)$, $a_2^j u_2(t - \lambda_j)$, and $a_3^{i,j} u_1(t - \kappa_i) u_2(t - \lambda_j)$. Thus, identifying this second-order input-only NARX model yields an optimal canonical representation of any PAC signal (Fig. 9).

The effective modulation (coupling) strength (i.e. the modulation depth or modulation index) can be quantified from the canonical approximation using the simulated output spectrum of the identified NARX model, $\hat{Z}(\omega)$ (similar to Figs. 3–5). Specifically, it is defined as the mean magnitude ratio of the intermodulation components at $\omega_F \pm \omega_S$ to the magnitude of the high-frequency component at ω_F . Accordingly, the PAC modulation index in the proposed NARX-based approach is

$$\text{MI} = \frac{\left| \hat{Z}(\omega_F + \omega_S) \right| + \left| \hat{Z}(\omega_F - \omega_S) \right|}{2 \left| \hat{Z}(\omega_F) \right|}. \quad (15)$$

The spectrum $\hat{Z}(\omega)$ is computed via a normalised fast Fourier transform (FFT) of the simulated output $z(t)$:

$$\hat{Z}(\omega) = \frac{T_s}{N} \text{FFT}\{z(t)\}, \quad (16)$$

where T_s is the sampling time ($T_s = 1/F_s$, with F_s the sampling frequency), and N is the number of samples in $z(t)$.

Similar to Figures 5, for monophasic PAC the intermodulation components at $\omega_F \pm \omega_S$ in the canonical approximation have magnitudes smaller than that of the high-frequency component at ω_F , whereas the opposite holds for biphasic PAC. Consequently, in (15), $\text{MI} < 1$ for monophasic coupling and $\text{MI} > 1$ for biphasic coupling, providing a straightforward interpretation of PAC type from this metric. Moreover, when $\text{MI} < 1$, the value reflects the effective modulation depth (Fig. 5A), whereas $\text{MI} > 1$ indicates the strength of biphasic coupling (Fig. 5B–C).

For the system identification algorithm to select the appropriate model terms that capture QPC and approximate a PAC signal in canonical form (equation (14)),

it is essential to specify suitable maximum delays for the two input terms, that is, the number of past input values considered [111]. This selection is analogous to defining the embedding window in time-delay embedding (embedding time window) [111]. In periodic dynamics, it is generally recommended to include delays covering up to one full period (or quasi-period) of the frequency of interest to adequately reconstruct the underlying dynamics [112, 113]. Based on extensive empirical evaluation, we found that a maximum delay of a quarter-period ($0.25(2\pi/\omega_S)$) for the slow oscillation and one full period ($2\pi/\omega_F$) for the fast oscillation provides a robust and effective configuration.

NARX model terms can be systematically grouped into *term clusters* according to their monomial structure [114, 115]. Each cluster represents a subset of terms with similar algebraic forms. For example, $u(t-1)u(t-3)$, $u(t-1)^2$, and $u(t-5)^2$ all belong to the cluster Σ_{uu} , which contains products of two delayed instances of the input $u(t)$. In a two-input, single-output NARX model, clusters such as $\Sigma_{u_1^2 u_2}$ or $\Sigma_{u_1 u_1 u_2}$ represent terms composed of two delays of $u_1(t)$ and one delay of $u_2(t)$. Importantly, different clusters correspond to distinct underlying dynamics [114–116]. Accordingly, linking equation (9) with equation (14), the terms in equation (14) can be grouped into term clusters as follows

$$\begin{aligned} a_1^i u_1(t - \kappa_i) &\in \Sigma_{u_1} \\ a_2^j u_2(t - \lambda_j) &\in \Sigma_{u_2} \\ a_3^{i,j} u_1(t - \kappa_i) u_2(t - \lambda_j) &\in \Sigma_{u_1 u_2} \end{aligned} \quad (17)$$

Therefore, it follows that in a second-order NARX model, PAC arises exclusively from the term clusters $\{\Sigma_{u_1}, \Sigma_{u_2}, \Sigma_{u_1 u_2}\}$.

The cluster Σ_{u_1} (including its model terms and parameters) represents the low-frequency component of the canonical approximation of a PAC signal, analogous to $x(t)$ in equation (1). The clusters $\{\Sigma_{u_2}, \Sigma_{u_1 u_2}\}$ encode the dynamics underlying the amplitude-modulated high-frequency component, analogous to $y(t + \delta t)$ in equation (1). In particular, $\Sigma_{u_1 u_2}$ specifically characterises QPC (equation (10)). By leveraging these properties of a second-order NARX model, the identified PAC dynamics can be explicitly decomposed into low-frequency and amplitude-modulated high-frequency components, as illustrated in Figure 10.

Building on the preceding formulation, the detection and characterisation of PAC in an unknown signal are performed by identifying second-order NARX models across a grid of low- and high-frequency pairs. A frequency pair is considered functionally coupled, and thus indicative of PAC, if the resulting NARX model includes the clusters $\{\Sigma_{u_1}, \Sigma_{u_2}, \Sigma_{u_1 u_2}\}$. However, noise and other phase-locked frequency components can occasionally induce spurious instances of PAC, resulting in

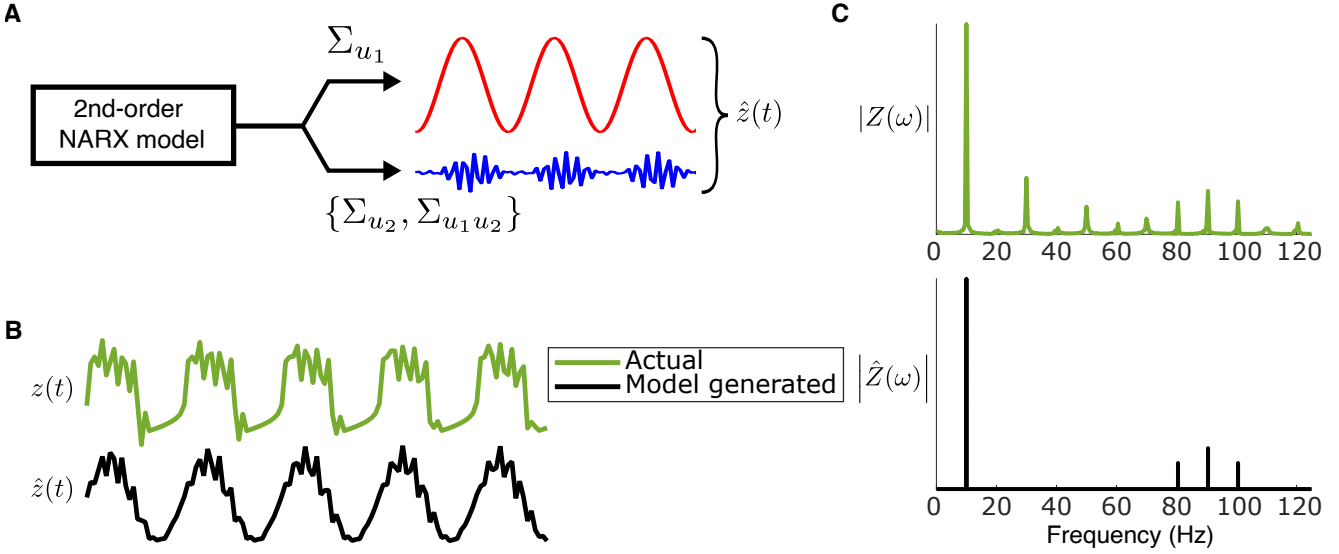


Figure 10. **Canonical approximation of a PAC signal using an identified 2nd-order NARX model.** The PAC signal is produced using the model given in equations (1) and (3) with a non-sinusoidal slow oscillation (equation (4)). As shown in **A**, for the identified 2nd-order NARX model, evaluating the response from just the term cluster Σ_{u_1} gives the low-frequency component while the response from the term clusters $\{\Sigma_{u_2}, \Sigma_{u_1 u_2}\}$ gives the high-frequency amplitude modulation component. Only the response from the clusters $\{\Sigma_{u_1} \Sigma_{u_2}, \Sigma_{u_1 u_2}\}$ is considered as the canonical approximation, $\hat{z}(t)$, of the actual PAC signal, $z(t)$. **B** shows the actual PAC signal, $z(t)$, and its canonical approximation generated by an identified 2nd-order NARX model. While the respective magnitude spectra of the actual PAC signal, $|Z(\omega)|$, and its canonical approximation from the identified NARX model, $|\hat{Z}(\omega)|$ are shown in **C**.

false positives. To mitigate this, additional empirically derived conditions are imposed, based on the spectrum of the model-generated output $\hat{Z}(\omega)$ (Fig. 10C):

1. The magnitudes at the frequencies ω_S and ω_F must be relatively significant with respect to each other.

$$a_1 < \frac{|\hat{Z}(\omega_F)|}{|\hat{Z}(\omega_S)|} < a_2 \quad (18)$$

where $a_1 = 0.04$ and $a_2 = 0.1$.

2. The magnitudes of the two intermodulation frequencies must be almost the same,

$$\frac{\min\left(\left|\hat{Z}(\omega_F + \omega_S)\right|, \left|\hat{Z}(\omega_F - \omega_S)\right|\right)}{\max\left(\left|\hat{Z}(\omega_F + \omega_S)\right|, \left|\hat{Z}(\omega_F - \omega_S)\right|\right)} \geq 0.7. \quad (19)$$

Condition 1 ensures two criteria are met: the magnitude of $\hat{Z}(\omega_F)$ is not too small relative to the magnitude of $\hat{Z}(\omega_S)$, and vice versa. This effectively rejects weak frequency components that are likely to arise from background noise. Condition 2 rejects spurious PAC that may occur due to noise or other phase-locked frequency components. It ensures that the magnitudes of

the two inter-modulating frequency components are approximately equal, within a prescribed tolerance. This symmetry is a key characteristic of the inter-modulation frequency components associated with genuine PAC (Figs. 3 and 4).

The proposed NARX-based PAC approach has so far been described in the context of stationary, sinusoidal or non-sinusoidal slow and fast oscillations (Figs. 9 and 10). However, real electrophysiological data rarely satisfy these assumptions. The following section outlines how the NARX-based PAC approach can be applied to real electrophysiological recordings.

D. Practical implementation

In realistic EEG and MEG recordings, the slow and fast oscillations underlying PAC are often highly non-stationary, i.e. their amplitude, frequency, and phase can vary over time [35, 45, 81]. For instance, the phase of a slow oscillation fluctuating between 5–6 Hz may modulate the amplitude of a fast oscillation whose frequency varies between 60–65 Hz. This can be expressed as $x(t) = A_S(t) \cos(\omega_S(t)t + \phi_S)$ for the slow oscillation, with $\omega_S(t) \in [5, 6]$, and $h(t) = \cos(\omega_F(t)t + \phi_F)$ for the fast oscillation, with $\omega_F(t) \in [60, 65]$. Under such non-stationary conditions, a system identification

approach based solely on stationary sinusoidal inputs $u_1(t)$ and $u_2(t)$ (see Sections III B and III C; Fig. 9) is insufficient to capture large fluctuations in amplitude, frequency, or phase.

In addition to non-stationarity, phase–amplitude coupled oscillations in real EEG and MEG data are often further contaminated by simultaneous electrophysiological activity from the same or neighbouring brain region. This background activity is commonly approximated as coloured noise, in particular pink noise [117–120]. Under these conditions, the proposed approach, when relying on idealised sinusoidal inputs for $u_1(t)$ and $u_2(t)$, struggles to accurately model signals with substantial pink noise contamination, particularly when the SNR is below 5.

A straightforward way to address both non-stationarity and noise is to apply bandpass filtering to the signal around the target low and high frequencies, and to use the resulting filtered signals as $u_1(t)$ and $u_2(t)$. Bandpass filtering is implemented via the FFT and inverse-FFT, which can be performed efficiently even on short signal segments (e.g. under 3 seconds). To reduce ringing effects from sharp filter windows (brick-wall filter), an FFT filter window with a smooth cosine roll-off is used. A 10% transition band for roll-off was empirically found to be sufficient.

The filtering bandwidth must be sufficiently wide to retain meaningful non-stationary features of the oscillatory signal, yet narrow enough to suppress unrelated neighbouring components that are not phase–amplitude coupled. In practice, for extracting the fast oscillation, a bandwidth of 1 Hz centred on the high-frequency of interest (ω_F , in radians per second) was found adequate, i.e. filtering between $(\omega_F/2\pi) \pm 0.5$ Hz. To extract the slow oscillation, filtering at the low-frequency of interest (ω_S , in radians per second) with a 1 Hz or 2 Hz bandwidth, i.e. between $(\omega_S/2\pi) \pm 0.5$ Hz and $(\omega_S/2\pi) \pm 1$ Hz, is generally adequate. However, to obtain accurate results, the filtering bandwidth should be close to the actual bandwidth of the slow oscillation that is phase–amplitude coupled and centred around ω_S .

Earlier, in Section III C, the maximum delay (embedding time window) required for system identification of stationary ideal slow-oscillation dynamics was one quarter-period. However, in practical applications, for accuracy and robustness, the maximum delay associated with the slow oscillation should be set to one half-period (π/ω_S). This enables robustness to non-stationarities, noise, and spurious coupling arising from other phase-locked frequency components.

The next section provides pseudocode outlining the core steps of the proposed methodology.

E. Procedures

Let $\zeta(t)$ denote the signal to be analysed for PAC, ω_1^R denote the slow oscillation filtering bandwidth, and let \wp_S and \wp_F respectively represent the slow and fast oscillation frequency query grid. Given these inputs, the proposed methodology produces a coupling map, referred to here as a comodulogram, denoted by \mathcal{C} .

The proposed NARX-based PAC method scans each frequency pair $\{\omega_1, \omega_2\}$ such that $\omega_1 \in \wp_S$, $\omega_2 \in \wp_F$, and $\omega_1 < \omega_2$. Here, ω_1 corresponds to the slow oscillation frequency and ω_2 to the fast oscillation frequency. For every pair $\{\omega_1, \omega_2\}$ that exhibits PAC, a canonical approximation is identified using a 2nd-order NARX model, denoted η . The model η includes the term clusters $\{\Sigma_{u_1}, \Sigma_{u_2}, \Sigma_{u_1 u_2}\}$, and its output spectrum satisfies the conditions in equations (18)–(19). Each resulting model is stored in \mathcal{M} , with $\mathcal{M}(\omega_1, \omega_2) = \eta$.

The comodulogram, \mathcal{C} , highlights frequency pairs, $\{\omega_1, \omega_2\}$, that exhibit PAC, with coupling strength indicated by $\mathcal{C}(\omega_1, \omega_2) > 0$. The corresponding 2nd-order NARX models, $\mathcal{M}(\omega_1, \omega_2)$, can then be used to quantify and interpret the nature of PAC between any identified coupled frequencies (see Fig. 10).

To reduce computational time, the method first performs an initial scan over the frequency grid (defined by \wp_S and \wp_F) to reduce the number of low–high frequency pairs $\{\omega_1, \omega_2\}$ that must be evaluated. This step identifies frequencies in $\zeta(t)$ that contain stable slow and fast oscillatory components. The scan uses linear autoregressive with exogenous input (ARX) model identification, which is substantially faster than fitting NARX models. For pairs $\{\omega_1, \omega_2\}$ exhibiting stable oscillatory components, the identified ARX model $\bar{\eta}$ contains only the term clusters $\{\Sigma_{u_1}, \Sigma_{u_2}\}$. These pairs are recorded in $\bar{\mathcal{C}}$ such that $\bar{\mathcal{C}}(\omega_1, \omega_2) = 1$ (and 0 otherwise). Only the shortlisted pairs with $\bar{\mathcal{C}}(\omega_1, \omega_2) = 1$ are then analysed in the final stage, where PAC is detected and characterised via system identification of second-order NARX models.

The core procedural steps for the initial scan are summarised in Algorithm 1, while the complete NARX-based PAC methodology is summarised in Algorithm 2. In both Algorithms 1 and 2, $\mathcal{F}(\zeta(t), \omega_a, \omega_b)$ denotes the bandpass-filtering of signal $\zeta(t)$ within the frequency range $[\omega_a, \omega_b]$ (see Section III D).

In Algorithm 2, SysIdNARX($\zeta(t), u_1(t), u_2(t), n_{b_1}, n_{b_2}$) denotes the system identification of a two-input single-output 2nd-order NARX model, given the output signal $\zeta(t)$ (the signal analysed for PAC), the two input signals $u_1(t)$ and $u_2(t)$ (the narrow-band filtered slow and fast oscillations, respectively; see Section III D), and the maximum numbers of past instances (embedding time window) of $u_1(t)$ and $u_2(t)$, n_{b_1} and n_{b_2} (see Appendix A). Similarly, in Algorithm

1, $\text{SysIdARX}(\zeta(t), u_1(t), u_2(t), n_{b_1}, n_{b_2})$ denotes the system identification of a two-input single-output linear ARX model.

Algorithm1 NARX-based PAC: Initial scan

```

1: Input:  $\zeta(t), \wp_S, \wp_F, \omega_1^R$ 
2: Initialise:  $\bar{C}$ 
3:  $\triangleright$  Filtering bandwidth for extracting the fast oscillation
4:  $\omega_2^R \leftarrow 0.5$ 
5: for  $\omega_1 \in \wp_S$  do
6:   for  $\omega_2 \in \wp_F$  do
7:     if  $\omega_1 < \omega_2$  then
8:        $u_1(t) \leftarrow \mathcal{F}(\zeta(t), \omega_1 - \omega_1^R, \omega_1 + \omega_1^R)$ 
9:        $u_2(t) \leftarrow \mathcal{F}(\zeta(t), \omega_2 - \omega_2^R, \omega_2 + \omega_2^R)$ 
10:       $n_{b_1} \leftarrow 0.5(2\pi/\omega_1)$ 
11:       $n_{b_2} \leftarrow \pi/\omega_2$ 
12:       $\bar{\eta} \leftarrow \text{SysIdARX}(\zeta(t), u_1(t), u_2(t), n_{b_1}, n_{b_2})$ 
13:      if  $\bar{\eta}$  contains  $\{\Sigma_{u_1}, \Sigma_{u_2}\}$  then
14:        if  $\bar{\eta}$  is stable then
15:           $\triangleright \omega_1$  and  $\omega_2$  are significant
16:           $\bar{C}(\omega_1, \omega_2) \leftarrow 1$ 
17:        else
18:           $\triangleright$  The pair  $\{\omega_1, \omega_2\}$  is not significant
19:           $\bar{C}(\omega_1, \omega_2) \leftarrow 0$ 
20:        end if
21:      else
22:         $\triangleright \omega_1$  and/or  $\omega_2$  is not significant
23:         $\bar{C}(\omega_1, \omega_2) \leftarrow 0$ 
24:      end if
25:    end if
26:  end for
27: end for
28: Output:  $\bar{C}$ 

```

To assess the statistical significance of PAC results, surrogate analysis is typically performed. For the NARX-based PAC methodology, this can be done by generating a set of surrogate datasets and processing them through Algorithm 2, one surrogate realisation at a time. Specifically, the input $\zeta(t)$ is replaced by a surrogate signal rather than the original data. To reduce computational cost, surrogate testing can be restricted to the frequency pairs identified as PAC candidates.

Section III C (Figs. 9 and 10) presented the NARX-based PAC method for the ideal case of stationary oscillations with discrete spectral peaks ($Z(\omega)$ in Figs. 3–4 and Fig. 10C). Section III D extends the method to the general case, where oscillations are non-stationary and spread around a centre frequency. However, neurological responses to periodic visual or auditory stimulation, such as steady-state visual evoked potentials (SSVEPs) or auditory steady-state responses (ASSRs), are frequency-locked to the stimulus and often exhibit extremely narrowband, near-stationary oscillations with sharp discrete spectral peaks, closely resembling the ideal case. Therefore, for SSVEPs and ASSRs, the earlier-mentioned ideal-case procedure should

be used. In this setting, Algorithms 1 and 2 should use $u_1(t) \leftarrow \cos(\omega_1 t)$, $u_2(t) \leftarrow \cos(\omega_2 t)$, and $n_{b_1} \leftarrow 0.25, (2\pi/\omega_1)$ (see Section III C).

Algorithm2 NARX-based PAC: Detection and quantification

```

1: Input:  $\zeta(t), \wp_S, \wp_F, \omega_1^R$ 
2: Initialise:  $\mathcal{C}, \mathcal{M}$ 
3:  $\bar{C} \leftarrow$  Run initial scan, Algorithm 1
4:  $\triangleright$  Filtering bandwidth for extracting the fast oscillation
5:  $\omega_2^R \leftarrow 0.5$ 
6: for  $\omega_1 \in \wp_S$  do
7:   for  $\omega_2 \in \wp_F$  do
8:     if  $\omega_1 < \omega_2$  then
9:        $\triangleright$  Check  $\{\omega_1, \omega_2\}$  has passed the initial scan
10:      if  $\bar{C}(\omega_1, \omega_2) = 1$  then
11:         $u_1(t) \leftarrow \mathcal{F}(\zeta(t), \omega_1 - \omega_1^R, \omega_1 + \omega_1^R)$ 
12:         $u_2(t) \leftarrow \mathcal{F}(\zeta(t), \omega_2 - \omega_2^R, \omega_2 + \omega_2^R)$ 
13:         $n_{b_1} \leftarrow 0.5(2\pi/\omega_1)$ 
14:         $n_{b_2} \leftarrow \pi/\omega_2$ 
15:         $\eta \leftarrow \text{SysIdNARX}(\zeta(t), u_1(t), u_2(t), n_{b_1}, n_{b_2})$ 
16:        if  $\eta$  contains  $\{\Sigma_{u_1}, \Sigma_{u_2}, \Sigma_{u_1 u_2}\}$  then
17:          if  $\eta$  is stable then
18:            Simulate  $\eta$  and extract response,
19:             $\hat{z}(t)$ , from only  $\{\Sigma_{u_1}, \Sigma_{u_2}, \Sigma_{u_1 u_2}\}$ .
20:            Evaluate  $\hat{Z}(\omega)$ 
21:            and MI, eqs. (15)-(16).
22:            if eqs. (18)-(19) are satisfied then
23:               $\triangleright \omega_1$  and  $\omega_2$  are coupled
24:               $\mathcal{C}(\omega_1, \omega_2) \leftarrow$  MI
25:               $\mathcal{M}(\omega_1, \omega_2) \leftarrow \eta$ 
26:            else
27:               $\triangleright \omega_1$  or  $\omega_2$  are uncoupled
28:               $\mathcal{C}(\omega_1, \omega_2) \leftarrow 0$ 
29:               $\mathcal{M}(\omega_1, \omega_2) \leftarrow 0$ 
30:            end if
31:          else
32:             $\triangleright \eta$  is unstable
33:             $\mathcal{C}(\omega_1, \omega_2) \leftarrow 0$ 
34:             $\mathcal{M}(\omega_1, \omega_2) \leftarrow 0$ 
35:          end if
36:        else
37:           $\triangleright \omega_1$  and  $\omega_2$  are uncoupled
38:           $\mathcal{C}(\omega_1, \omega_2) \leftarrow 0$ 
39:           $\mathcal{M}(\omega_1, \omega_2) \leftarrow 0$ 
40:        end if
41:      else if
42:         $\triangleright \omega_1$  and  $\omega_2$  are uncoupled
43:         $\mathcal{C}(\omega_1, \omega_2) \leftarrow 0$ 
44:         $\mathcal{M}(\omega_1, \omega_2) \leftarrow 0$ 
45:      end if
46:    end if
47:  end for
48: end for
49: Output:  $\mathcal{C}, \mathcal{M}$ 

```

It should be noted that polynomial NARX model identification in this study was carried out using the open-source MATLAB package *NonSysID* [108, 109],

which includes built-in simulation stability checks. Therefore, the stability checks required in line 14 of Algorithm 1 and line 17 of Algorithm 2 are inherently satisfied.

IV. EXPERIMENTAL RESULTS

This section presents a systematic comparative evaluation of the proposed NARX-based framework for PAC detection and characterisation against several established benchmark methods. The evaluation utilises both synthetic and real electrophysiological datasets. Synthetic datasets are generated according to the models described in Section II A, while benchmark comparisons include filtering-based PAC metrics introduced by Ozkurt *et al.* [47], Canolty *et al.* [45], and Penny *et al.* [46].

The synthetic data experiments are designed to assess the specificity and robustness of the proposed approach under controlled conditions. Of the two analytical models introduced in Section II A, we focus on the model defined by equations (1) and (3). This model is preferred because it generates non-sinusoidal amplitude modulation, thereby producing additional phase-locked spectral components—conditions well-suited for testing robustness against spurious coupling. It also simulates PAC patterns in which high-frequency oscillations emerge and fade around a specific phase of the low-frequency signal, with gradual tapering at the onset and offset (Fig. 4D), closely reflecting the dynamics observed in NMMs (Fig. 6) and in empirical neurophysiological recordings.

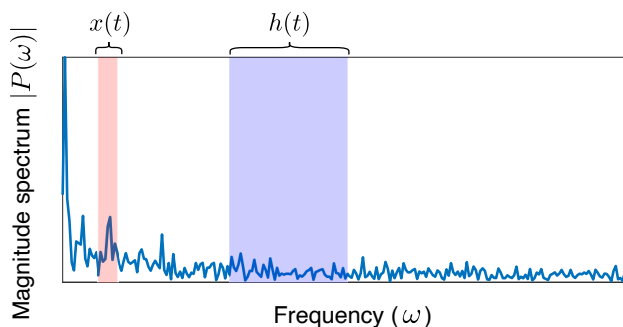


Figure 11. **Generating non-stationary slow and fast oscillations.** To obtain non-stationary slow and fast oscillations $x(t)$ and $h(t)$, respectively, a randomly generated pink noise sample $p(t)$ is bandpass-filtered in the frequency ranges of interest. This is illustrated using the magnitude spectrum $|P(\omega)|$ of a pink noise sample $p(t)$. The red and blue shaded regions indicate the frequency ranges of interest for the non-stationary slow, $x(t)$, and fast, $h(t)$, oscillations.

As noted in Section III D, real electrophysiological signals are inherently non-stationary. Moreover, the

spectral profile of EEG and MEG often resembles pink noise, with magnitude inversely proportional to frequency [117–120]. It is therefore critical that the proposed method can handle both non-stationarities and pink noise. In our simulations, white noise was generated and converted into pink noise by shaping its spectrum so that the magnitude decreased inversely with frequency (Fig. 11). Subsequently, non-stationary oscillations were generated by bandpass filtering of random pink noise. All synthetic datasets used in this section were produced following this procedure.

For all experiments, the PAC model (equations (1) and (3)) was used. Each synthetic time series was 10 seconds long, which is generally considered the minimum time window required for robust PAC analysis using filtering-based PAC methods [52, 121]. Filtering is more accurate at high sampling rates. Therefore, to maintain accuracy in filtering-based methods and to generate high-quality synthetic PAC signals (Fig. 11), a sampling frequency of 1000 Hz was used. For system identification, appropriate down-sampling is required to maintain accuracy [122, 123]. Consequently, the generated synthetic PAC signal was down-sampled to 250 Hz for the proposed NARX-based PAC method.

Three synthetic datasets were generated using the selected analytical model:

1. A basic sinusoidal case with coupling between a 7 Hz slow oscillation and a 63 Hz fast oscillation.
2. A case with a 6–7 Hz slow oscillation coupled to a fast oscillation ranging from 55–60 Hz.
3. A more complex case where a slow oscillation ranging from 9–10 Hz is simultaneously coupled to two distinct high-frequency bands: 40–45 Hz and 65–75 Hz.

To simulate realistic conditions, a sample of pink noise was added to the generated PAC signal, yielding an SNR of approximately 9.5 dB (≈ 3), where the noise variance was set to be $\approx 33\%$ of the signal. Experiments 2 and 3 are particularly useful for assessing the method’s ability to detect PAC under broadband oscillatory components and non-stationary conditions. Furthermore, to demonstrate the repeatability and specificity of our approach, we average the comodulograms obtained from multiple realisations of the same PAC signal (cases 2 and 3 above), each generated using a different pink-noise sample (i.e. different random-number-generator seeds). Detailed descriptions for each setup and the corresponding results are provided in the following sections.

A. Single frequency oscillations with non-sinusoidal amplitude modulation

The first simulated PAC example, shown in Figure 12, involves a 7 Hz slow oscillation coupled with a 63 Hz high-frequency sinusoidal oscillation. Figure 12A displays a short segment of the simulated signal $z(t)$ alongside its magnitude spectrum $|Z(\omega)|$. As expected, the spectrum contains intermodulation components at 56 Hz and 70 Hz, as well as several other phase-locked components. Many of these are integer multiples of the 7 Hz base frequency, raising the potential for spurious couplings. Notably, the 63 Hz component itself is such a multiple. Nevertheless, the experiment shows that the proposed method accurately identifies genuine PAC while robustly rejecting spurious couplings with high specificity.

After constructing the comodulogram (Fig. 12B), a more detailed examination of the identified couplings can be carried out, as shown in Figure 13. Figure 13B compares the original PAC signal with the canonical approximation generated by the NARX model (see Sections III B and III C). The NARX models for each detected coupling can also be decomposed into their constituent components—the slow oscillation and the amplitude-modulated fast oscillation (as illustrated in Fig. 10).

Figure 13B shows both the actual and the model-generated slow and fast oscillatory components. Since the canonical approximation consists of purely sinusoidal components (see Section III B), the Hilbert transform can be applied directly—without additional narrowband filtering—to extract instantaneous phase information. The relationship between the phase of the slow oscillation and the amplitude envelope of the fast oscillation is visualised using a phase-amplitude histogram [44], where the slow-phase cycle is divided into bins and the mean fast-amplitude within each bin is computed. As shown in Figure 13C for both the actual signal and the canonical approximation, this procedure reveals the slow-phase at which the fast oscillation reaches its peak amplitude. Taken together, Figures 13B–C demonstrate that the NARX-based method accurately identifies the phase of fast oscillatory bursts, confirming its effectiveness for PAC characterisation.

B. Non-stationary oscillations and pink noise

A slow oscillation in the 6–7 Hz range and a fast oscillation in the 55–60 Hz range were extracted via bandpass filtering of pink noise (Fig. 11). These components were phase-amplitude coupled using the analytical model with non-sinusoidal amplitude modulation (equations (1) and (3)). The resulting comodulograms,

comparing the proposed method with conventional approaches, are shown in Figure 14. For the conventional filtering-based methods, a sampling frequency of 1000 Hz was used, as filtering is better at higher sampling rates. For the proposed NARX-based PAC method, a sampling frequency of 250 Hz was used because this was the optimal sampling rate for the high frequencies considered. Furthermore, the slow oscillation filter bandwidth for the NARX-based method was set to 1 Hz (ω_1^R in Algorithms 1 and 2). A more complex scenario, with the same sampling rates as before, is illustrated in Figure 15, where a 9–10 Hz oscillation is simultaneously coupled to two distinct high-frequency bands: 40–45 Hz and 65–75 Hz.

The supplementary Figures 19 and 20 (see Appendix C) illustrate the reproducibility and specificity of the proposed NARX-based method. Figure 19 corresponds to Figure 14, in which 100 realisations of a PAC signal (6–7 Hz coupled with 55–60 Hz) were generated using 100 different pink-noise samples (Fig. 11). This yields 100 comodulograms. Figure 14 compares the average of these 100 comodulograms across the different methods. Similarly, Figure 20 corresponds to Figure 15.

From both examples (Figs. 14, 15, 19 and 20), the proposed method accurately identifies the coupled frequency bands and localises them to the regions of the comodulogram where genuine phase-amplitude interactions occur. In contrast, conventional filtering-based methods yield broader, less precise coupling profiles, characterised by increased frequency smearing and a higher susceptibility to false positives.

C. Evaluating performance on signals prone to spurious PAC

Sharp periodic waveforms (spike trains), which contain phase-locked harmonics, are frequently observed in the oscillatory frequency bands of electrocorticography (ECoG) data, especially in sensorimotor regions [54]. These signals manifest as sharp, periodic deflections rather than smooth oscillations. In many conventional PAC measures, such harmonics can generate spurious yet statistically significant PAC [54]. Figure 16 compares the proposed NARX-based PAC detection method with several standard techniques, using a simulated spike train signal generated according to the procedures described in [54].

D. Actual LFP data from the rat hippocampus

Scheffer-Teixeira et al. [124] analysed LFPs recorded from the CA1 region of the rat hippocampus during different sleep-wake states, including REM sleep and active wakefulness. Signals were sampled at

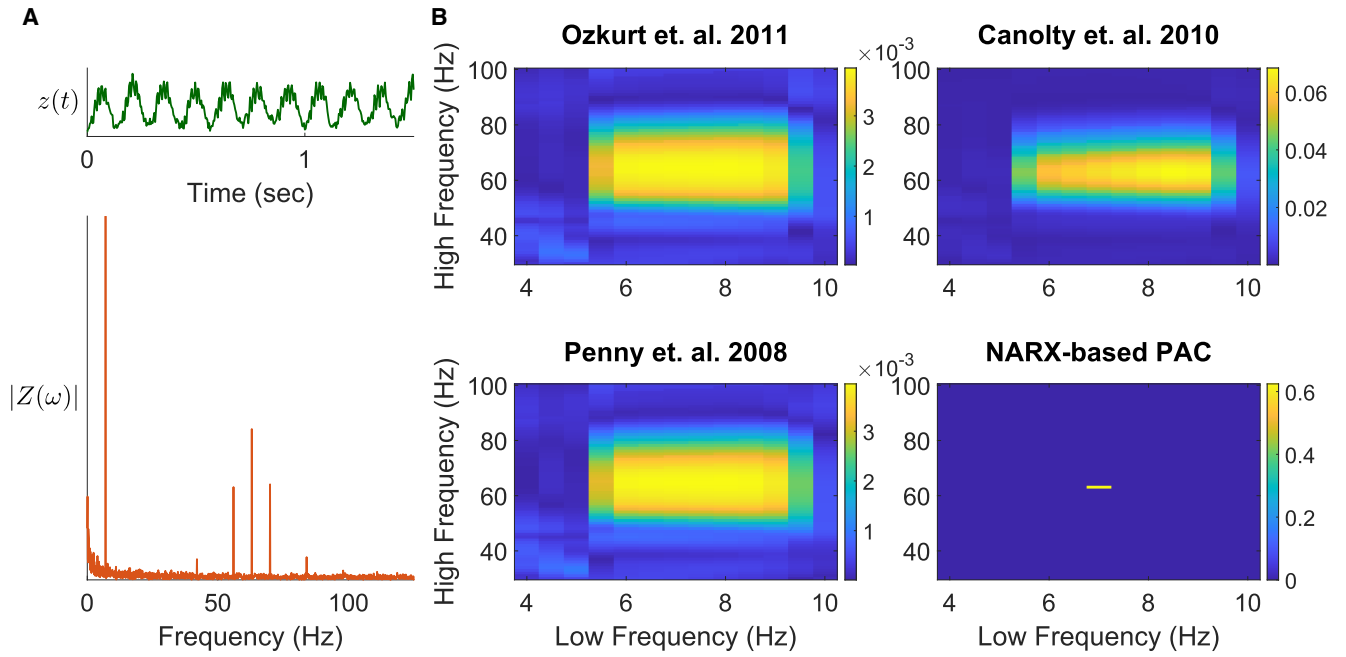


Figure 12. **Sinusoidal slow and fast oscillations are coupled using a non-sinusoidal amplitude modulation.** A 7 Hz slow oscillation is coupled with a 63 Hz fast oscillation to obtain the 10-second PAC signal $z(t)$. Panel A displays a segment of the signal $z(t)$ alongside its magnitude spectrum $|Z(\omega)|$. Panel B compares the proposed NARX-PAC method with alternative methods, using the comodulogram evaluated from each method.

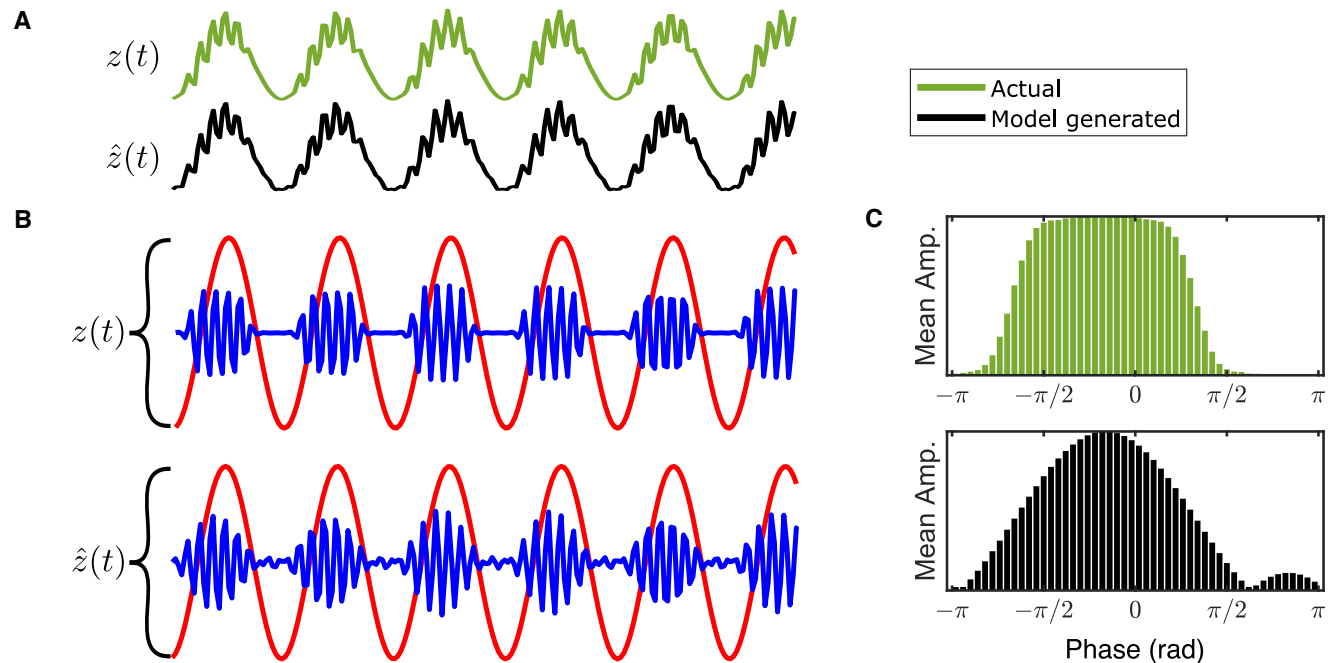


Figure 13. **PAC analysis using the proposed method.** This figure demonstrates the level of detail achievable in PAC analysis with the proposed method. The analysis corresponds to the synthetic experiment presented in Figure 12, where sinusoidal oscillations of 7 Hz and 63 Hz are coupled. **A** compares the true PAC signal $z(t)$ with the canonical approximation produced by the NARX model, $\hat{z}(t)$. **B** shows comparisons between the low-frequency (red) and the high-frequency amplitude modulation (blue) components of $z(t)$ and $\hat{z}(t)$. In **C**, the histograms illustrate how, for both $z(t)$ and $\hat{z}(t)$, the amplitude envelope of the modulated fast oscillation varies with the phase of the slow oscillation.

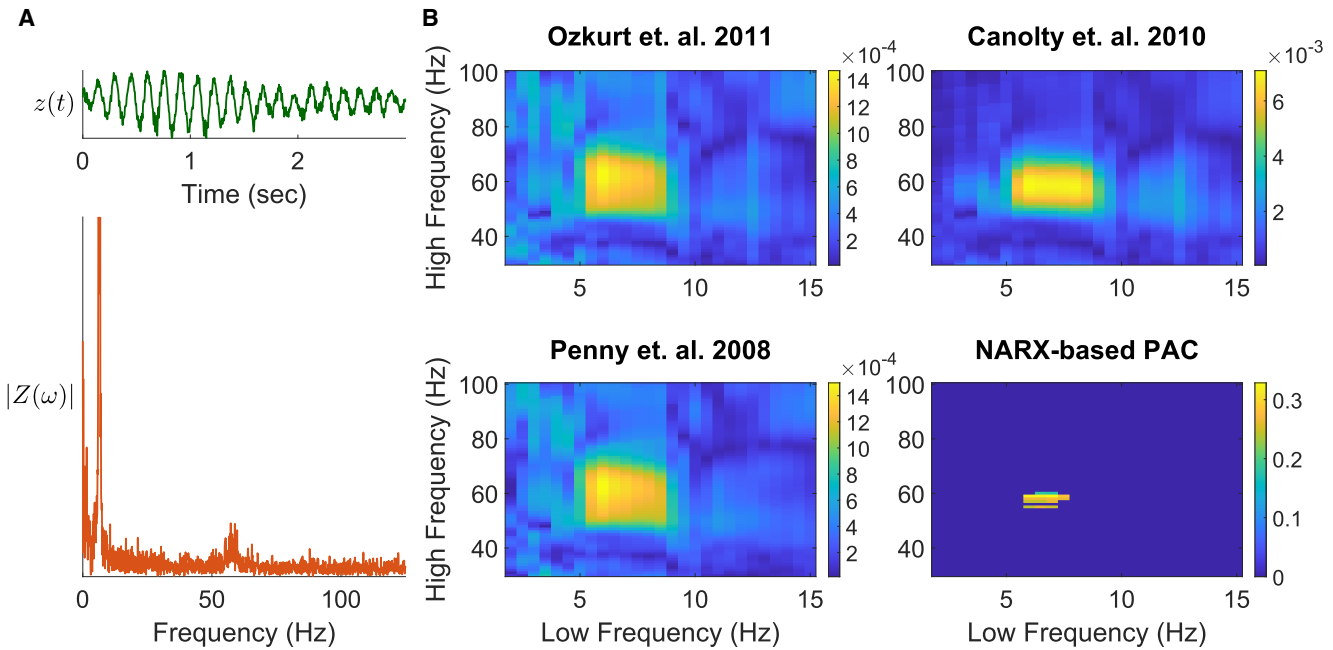


Figure 14. **Non-stationary slow oscillation coupled to non-stationary fast oscillation using a non-sinusoidal amplitude modulation.** A 6–7 Hz slow oscillation is coupled with 55–60 Hz non-stationary fast oscillations to obtain the 10-second PAC signal $z(t)$. **A** shows a snippet of the signal $z(t)$ and its magnitude spectrum $|Z(\omega)|$. Comparisons between the proposed NARX-PAC method and other methods are shown in **B** using the comodulogram evaluated from each method.

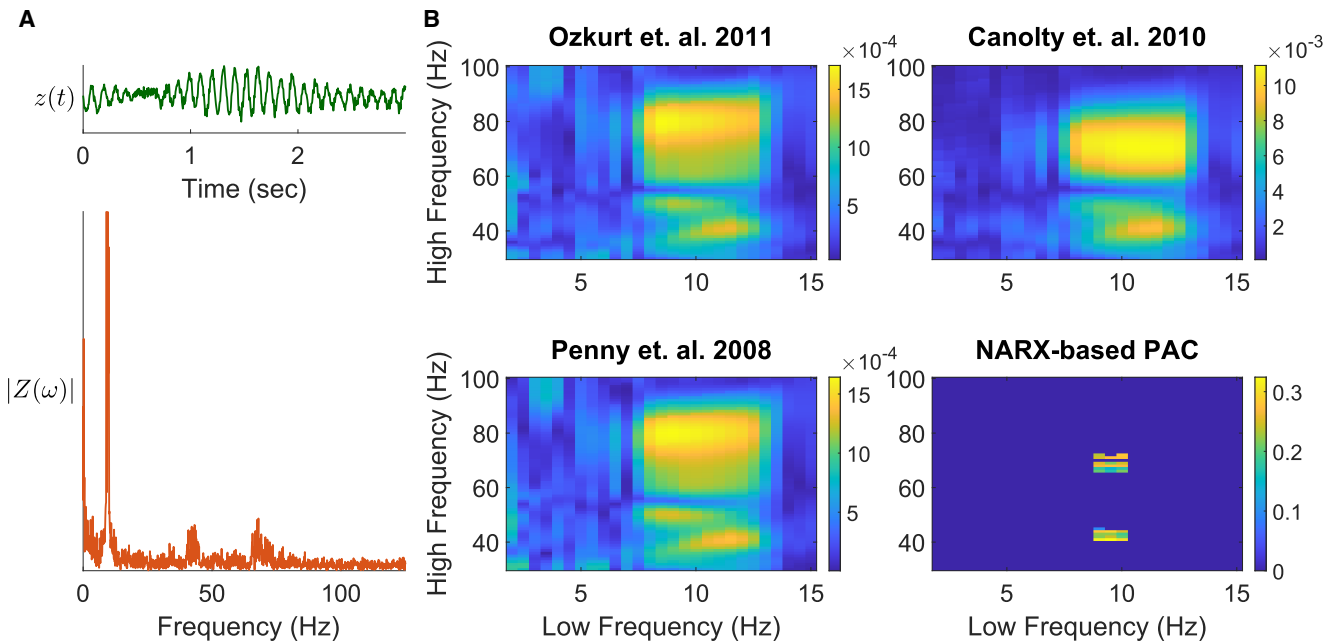


Figure 15. **Non-stationary slow oscillation coupled to two distinct non-stationary fast oscillations using a non-sinusoidal amplitude modulation.** A 9–10 Hz slow oscillation is coupled with 40–45 Hz and 65–75 Hz non-stationary fast oscillations to obtain the 10-second PAC signal $z(t)$. **A** shows a snippet of the signal $z(t)$ and its magnitude spectrum $|Z(\omega)|$. Comparisons between the proposed NARX-PAC method and other methods are shown in **B** using the comodulogram evaluated from each method.

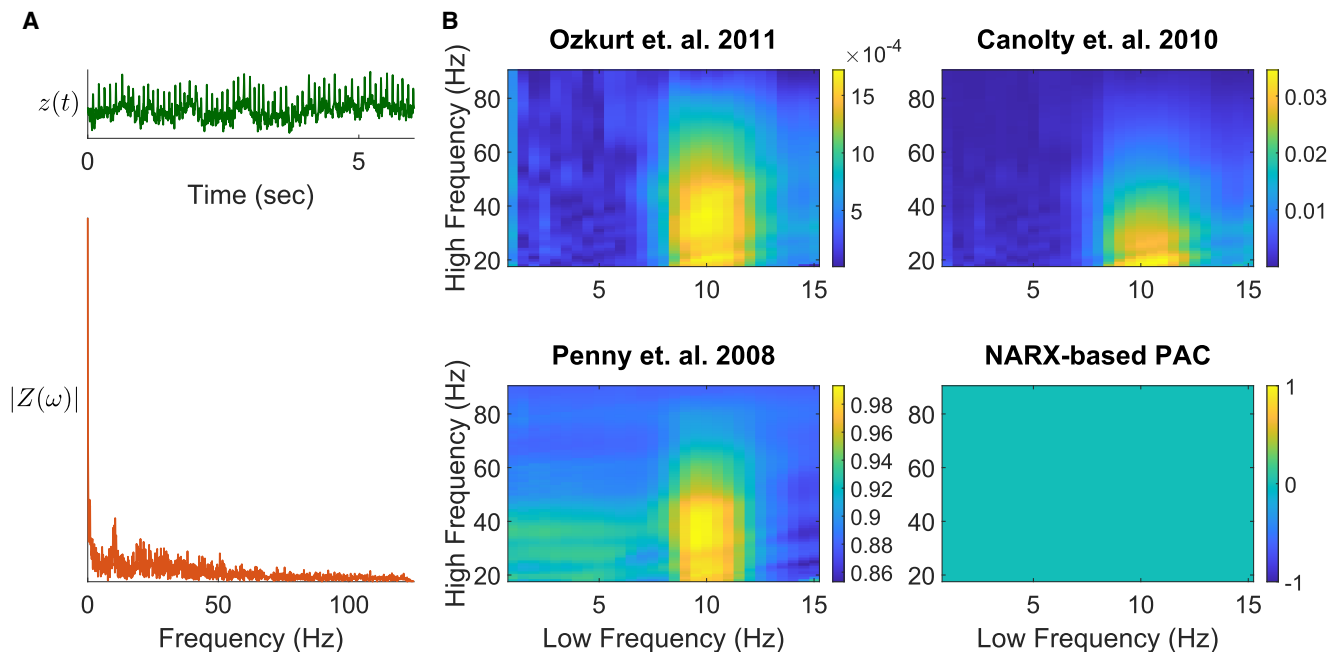


Figure 16. **Comparison using a simulated spike-train signal that produces spurious PAC.** Using the procedures mentioned in [54], a 10-second Gaussian-shaped periodic spike (spike-train) signal $z(t)$ is used here to compare how the proposed method can reject spurious couplings. **A** shows a snippet of the signal $z(t)$ and its magnitude spectrum $|Z(\omega)|$. Comparisons between the proposed NARX-PAC method and other methods are shown in **B** using the comodulogram evaluated from each method.

1000 Hz, and PAC was assessed using the modulation index proposed by Tort et al. [8, 44]. The study found that the low-frequency theta phase modulated two distinct high-frequency oscillations: (1) high-gamma (HG) oscillations around 80 Hz, predominant in deep CA1 layers (stratum lacunosum-moleculare), and (2) high-frequency oscillations (HFOs) around 140 Hz, which were dominant in superficial CA1 layers (stratum oriens-alveus). In the original study [124], HG and HFO were used specifically to distinguish these frequency bands; here, HFO refers to this higher gamma-band activity and should not be confused with the broader use of “high-frequency oscillation” elsewhere in this paper.

Two sample LFP recordings from the REM sleep state, originally reported in [124], are available via the GitHub repository [125]. One recording originates from deep CA1 layers (stratum lacunosum-moleculare), where high-gamma activity is prominent, and the other from superficial CA1 layers (stratum oriens-alveus), where HFOs dominate. These recordings were analysed using the proposed NARX-based method and were compared with conventional filtering-based approaches. For conventional methods, a sampling rate of 1000 Hz was used. For the NARX-based method, a sampling rate of 500 Hz was used. Furthermore, the slow oscillation filter bandwidth for the NARX-based method was set

to 0.5 Hz (ω_1^R in Algorithms 1 and 2).

Figure 17 shows the detected PAC frequency bands, and Figure 18 depicts the phase-coupling relationships associated with the 8 Hz low-frequency component. From the comodulograms in Figure 17, the NARX-based method appears sharper, providing more precise localisation of coupling. Figure 18 compares the phase information associated with the coupling—specifically, the phase of the low-frequency oscillation at which the high-frequency amplitude envelope peaks. As shown in Figure 18B, the NARX-based method can accurately identify the phase of the coupling.

V. DISCUSSION

PAC, a form of CFC, is thought to play a critical role in cognitive functions such as attention and consciousness, as well as in processes including information encoding, retrieval, maintenance, and large-scale neural communication. Accurate detection and characterisation of PAC are therefore essential for understanding brain function. Despite growing interest, reliable detection and interpretation remain challenging [51, 52]. In this study, we introduce a method rooted in the temporal dynamics that generate PAC. Specifically, we identify a nonlinear dynamical model that captures the es-

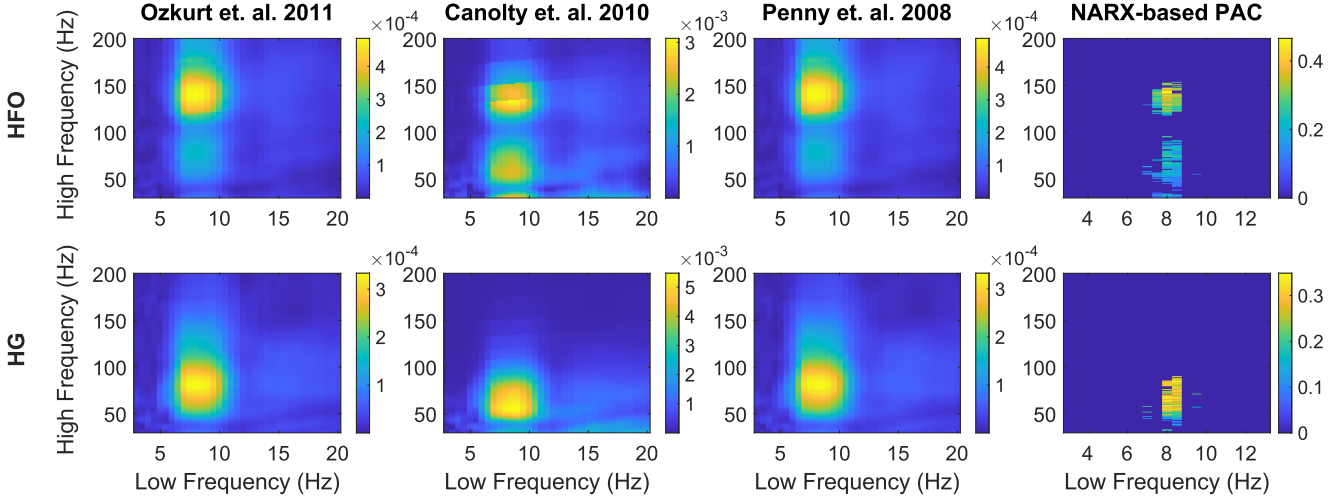


Figure 17. Comparison of PAC results between commonly used methods and the proposed NARX-PAC method on the LFP data from [124, 125]. PAC results are shown for the two LFPs that were provided in [125]. One of the LFP samples contains dominant frequencies around the HFO gamma frequency range (superficial CA1 layers, stratum oriens–alveus) and the other contains frequencies around the HG frequency range (deeper CA1 layers, stratum lacunosum–moleculare).

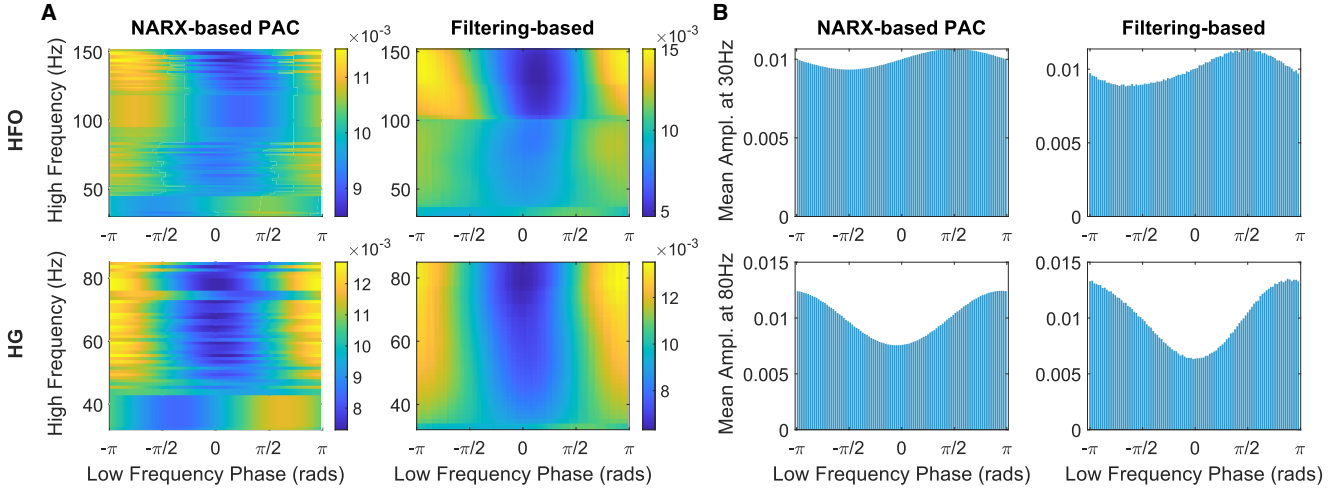


Figure 18. Comparison of phase information for the detected PACs at the low-frequency 8 Hz. From the detected PACs shown in Figure 17, this figure compares the phase information of all PACs involving the 8 Hz low-frequency component between the proposed NARX-based PAC method and the filtering-based PAC detection methods. Panel A shows comparisons of phase information for all couplings involving the 8 Hz low-frequency component. In contrast, panel B shows the comparison for a particular high-frequency coupling involving the 8 Hz low-frequency component.

sential dynamics of a PAC signal and can be simulated to reproduce its canonical form. Unlike approaches that focus solely on temporal fluctuations, this dynamical systems perspective provides several key advantages, as outlined in this section.

A. Discussion of the results

The proposed NARX-based method captures PAC dynamics in the form of a generative model, even under high-noise conditions. This is a key advantage, as it enables noise-free simulation of the learned dynamics, allowing detailed post-hoc analysis—a feature not offered by existing methods. As a result, critical properties of PAC, such as preferred phase, modulation strength, and

even coupling directionality (see [14]), can be reliably estimated.

The NARX-based method also provides a naturally normalised measure of coupling strength, without requiring additional scaling. This is achieved by quantifying coupling strength using a normalised FFT (equation (16)) of the simulated output from the NARX model that captures PAC dynamics (canonical approximation). The identified NARX model is simulated using stationary cosine inputs with the same variance as the filtered slow and fast oscillations ($u_1(t)$ and $u_2(t)$ respectively, Section III E). Simulating the canonical PAC dynamics in this way allows coupling strength to be evaluated without needing to account for variations in actual slow-oscillation amplitude. Furthermore, the proposed method yields sharper, more specific coupling localisation and improved robustness relative to commonly used filtering-based PAC measures (Figs. 19 and 20).

A major challenge in PAC analysis is the risk of spurious coupling detection [50, 51, 54, 83, 126, 127]. As noted in Section II D, spurious PAC can arise from non-sinusoidal waveforms or sharp transitions in slow oscillations, which introduce high-frequency harmonic components that are phase-locked to the fundamental frequency. The robustness of the proposed method against such artefacts was demonstrated in Section IV C. The spike-train signal in Figure 16 produces significant spurious PAC across all standard metrics, whereas the NARX-based approach successfully avoids false detection. Notably, this signal has also been shown to cause false positives in more recent methods [50, 83], further highlighting the robustness of the proposed framework.

The methodology presented by Tour *et al.* [83] shares conceptual similarities with the approach presented here. Their framework employs nonlinear autoregressive models to capture QPC, but it focuses exclusively on modelling the amplitude modulation component of a PAC signal. By contrast, the NARX-based method introduced here models the entire PAC signal, consistent with the analytical formulations described in Section II A.

B. Limitations and future work

This study demonstrates that a dynamical systems approach to PAC detection and characterisation via nonlinear system identification is both advantageous and practically feasible. This also creates opportunities for developing further methods grounded in the same principles. Nonetheless, the NARX-based approach presented here does have certain limitations.

The most evident limitation of the proposed method is its computational cost. A separate two-input, single-output NARX model must be identified for each low-

and high-frequency pair in the comodulogram. A potential solution is to use a multi-input, single-output NARX model that incorporates multiple low- and high-frequency inputs simultaneously. This would allow a single model to evaluate all frequency pairs, thereby greatly reducing the computational overhead.

In this study, a second-order NARX model was used to capture PAC dynamics, represented by the term clusters $\{\Sigma_{u_1}, \Sigma_{u_2}, \Sigma_{u_1 u_2}\}$ (see Section III C). Extending the model to include higher-order term clusters, such as $\{\Sigma_{u_1^2 u_2}, \Sigma_{u_1^3 u_2}, \Sigma_{u_1^2 u_2^3}\}$, would enable it to account for higher-order intermodulations. Within the iFRO identification framework, this would allow the modelling of non-sinusoidal amplitude modulations. Although such non-sinusoidal waveforms are not essential for characterising PAC (Section III B), they may carry additional physiological significance [85]. Characterising these features could therefore further advance the analysis of PAC. In addition, this extension may improve the ability to capture QPC when significantly stronger higher-order nonlinearities are present. However, caution is required when introducing nonlinear cross-terms beyond second-order between the low-frequency input u_1 and the high-frequency input u_2 , as these terms may also capture higher-order phase-coupling effects unrelated to QPC, potentially compromising its accurate identification. Nevertheless, this remains a promising direction for further advancing NARX-based PAC analysis.

As described in Section III D, the bandpass filters used to isolate low- and high-frequency oscillations—the two inputs to the NARX model—were configured with empirically determined fixed bandwidths. This configuration proved effective within the scope of the current study. However, with regard to isolating the slow oscillation, performance might be improved with a data-driven, adaptive bandwidth selection procedure, such as that proposed in [83], where bandwidth is estimated as a function of the oscillation’s centre frequency. Furthermore, the optimal sampling rates for system identification in the NARX-based PAC method should be investigated, as this depends on the considered fast-oscillation frequency.

The conditions for avoiding spurious couplings in equations (18) and (19) were derived empirically using several synthetically generated datasets containing both genuine and spurious PAC. However, these tolerances may not remain valid as the power of the fast oscillation approaches that of the slow oscillation, a major limitation of the current approach. Ideally, the criteria for excluding spurious couplings should be derived from underlying dynamical properties rather than established empirically. Addressing this issue should therefore be a priority in future research on the proposed method.

ACKNOWLEDGEMENTS

RG and FH were supported by EPSRC grant [EP/X020193/1].

-
- [1] G. Deco, V. K. Jirsa, P. A. Robinson, M. Breakspear, and K. Friston, "The dynamic brain: From spiking neurons to neural masses and cortical fields," *PLOS Computational Biology*, vol. 4, pp. 1–35, 08 2008.
- [2] A. Ghosh, Y. Rho, A. R. McIntosh, R. Kötter, and V. K. Jirsa, "Cortical network dynamics with time delays reveals functional connectivity in the resting brain," *Cognitive Neurodynamics*, vol. 2, pp. 115–120, Jun 2008.
- [3] E. Florin and S. Baillet, "The brain's resting-state activity is shaped by synchronized cross-frequency coupling of neural oscillations," *NeuroImage*, vol. 111, pp. 26–35, 2015.
- [4] E. Florin and S. Baillet, "Commentary: Evaluation of phase-amplitude coupling in resting state magnetoencephalographic signals: Effect of surrogates and evaluation approach," *Frontiers in Computational Neuroscience*, vol. Volume 12 - 2018, 2018.
- [5] G. Buzsáki, *Rhythms of the Brain*. Oxford University Press, 10 2006.
- [6] A. Hyafil, A.-L. Giraud, L. Fontolan, and B. Gutkin, "Neural cross-frequency coupling: Connecting architectures, mechanisms, and functions," *Trends in Neurosciences*, vol. 38, no. 11, pp. 725–740, 2015.
- [7] R. T. Canolty and R. T. Knight, "The functional role of cross-frequency coupling," *Trends in Cognitive Sciences*, vol. 14, no. 11, pp. 506–515, 2010.
- [8] A. B. L. Tort, M. A. Kramer, C. Thorn, D. J. Gibson, Y. Kubota, A. M. Graybiel, and N. J. Kopell, "Dynamic cross-frequency couplings of local field potential oscillations in rat striatum and hippocampus during performance of a t-maze task," *Proceedings of the National Academy of Sciences*, vol. 105, no. 51, pp. 20517–20522, 2008.
- [9] A. B. L. Tort, R. W. Komorowski, J. R. Manns, N. J. Kopell, and H. Eichenbaum, "Theta-gamma coupling increases during the learning of item-context associations," *Proceedings of the National Academy of Sciences*, vol. 106, no. 49, pp. 20942–20947, 2009.
- [10] M. X. Cohen, "Assessing transient cross-frequency coupling in eeg data," *Journal of Neuroscience Methods*, vol. 168, no. 2, pp. 494–499, 2008.
- [11] K. J. Friston, "The labile brain. i. neuronal transients and nonlinear coupling," *Philosophical Transactions of the Royal Society of London. Series B: Biological Sciences*, vol. 355, no. 1394, pp. 215–236, 2000.
- [12] M. Chehelcheraghi, C. van Leeuwen, E. Steur, and C. Nakatani, "A neural mass model of cross-frequency coupling," *PLOS ONE*, vol. 12, pp. 1–19, 04 2017.
- [13] V. Jirsa and V. Müller, "Cross-frequency coupling in real and virtual brain networks," *Frontiers in Computational Neuroscience*, vol. 7, 2013.
- [14] H. Jiang, A. Bahramisharif, M. A. van Gerven, and O. Jensen, "Measuring directionality between neuronal oscillations of different frequencies," *NeuroImage*, vol. 118, pp. 359–367, 2015.
- [15] B. Nandi, P. Swiatek, B. Kocsis, and M. Ding, "Inferring the direction of rhythmic neural transmission via inter-regional phase-amplitude coupling (ir-pac)," *Scientific Reports*, vol. 9, p. 6933, May 2019.
- [16] O. Jensen and L. L. Colgin, "Cross-frequency coupling between neuronal oscillations," *Trends in Cognitive Sciences*, vol. 11, no. 7, pp. 267–269, 2007.
- [17] S. Sadaghiani, M. J. Brookes, and S. Baillet, "Connectomics of human electrophysiology," *NeuroImage*, vol. 247, p. 118788, 2022.
- [18] U. Frieese, M. Köster, U. Hassler, U. Martens, N. Trujillo-Barreto, and T. Gruber, "Successful memory encoding is associated with increased cross-frequency coupling between frontal theta and posterior gamma oscillations in human scalp-recorded eeg," *NeuroImage*, vol. 66, pp. 642–647, 2013.
- [19] X. Wang, X. Cui, C. Ding, D. Li, C. Cheng, B. Wang, and J. Xiang, "Deficit of cross-frequency integration in mild cognitive impairment and alzheimer's disease: A multilayer network approach," *Journal of Magnetic Resonance Imaging*, vol. 53, no. 5, pp. 1387–1398, 2021.
- [20] F. Fraga, T. Falk, P. Kanda, and R. Anghinah, "Characterizing Alzheimer's disease severity via resting-awake EEG amplitude modulation analysis," *PLoS one*, vol. 8, p. e72240, 08 2013.
- [21] N. Jackson, S. R. Cole, B. Voytek, and N. C. Swann, "Characteristics of waveform shape in parkinson's disease detected with scalp electroencephalography," *eNeuro*, vol. 6, no. 3, 2019.
- [22] M. Muthuraman, M. Bange, N. Koirala, D. Ciolac, B. Pintea, M. Glaser, G. Tinkhauser, P. Brown, G. Deuschl, and S. Groppa, "Cross-frequency coupling between gamma oscillations and deep brain stimulation frequency in parkinson's disease," *Brain*, vol. 143, pp. 3393–3407, 11 2020.
- [23] D. Klepl, F. He, M. Wu, D. J. Blackburn, and P. G. Sarrigiannis, "Cross-frequency multilayer network analysis with bispectrum-based functional connectivity: A study of alzheimer's disease," *Neuroscience*, vol. 521, pp. 77–88, 2023.
- [24] X. Chen, Y. Li, R. Li, X. Yuan, M. Liu, W. Zhang, and Y. Li, "Multiple cross-frequency coupling analysis of resting-state eeg in patients with mild cognitive impairment and alzheimer's disease," *Frontiers in Aging Neuroscience*, vol. Volume 15 - 2023, 2023.
- [25] M. G. Mariscal, E. Berry-Kravis, J. D. Buxbaum, L. E. Ethridge, R. Filip-Dhima, J. H. Foss-Feig, A. Kolev-

- zon, M. E. Modi, M. W. Mosconi, C. A. Nelson, C. M. Powell, P. M. Siper, L. Soorya, A. Thaliath, A. Thurm, B. Zhang, M. Sahin, A. R. Levin, and the Developmental Synaptopathies Consortium, "Shifted phase of eeg cross-frequency coupling in individuals with phelan-mcdermid syndrome," *Molecular Autism*, vol. 12, p. 29, Apr 2021.
- [26] E. Ganiti-Roumeliotou, I. Ziogas, C. Lamprou, G. Alhussein, H. Alfalahi, A. A. Shehhi, S. Dias, H. F. Jelinek, T. Stouraitis, and L. J. Hadjileontiadis, "Classification of children with adhd through task-related eeg recordings via swarm-decomposition-based phase locking value," in *2023 45th Annual International Conference of the IEEE Engineering in Medicine & Biology Society (EMBC)*, pp. 1–5, 2023.
- [27] W. Tang, J. Jiang, and H. Wang, "Brain functional differences among adhd subtypes in children revealed by phase-amplitude coupling analysis of resting-state eeg," *International Journal of Psychophysiology*, vol. 215, p. 113222, 2025.
- [28] S. Hirano, A. Nakhnikian, Y. Hirano, N. Oribe, S. Kanba, T. Onitsuka, M. Levin, and K. M. Spencer, "Phase-amplitude coupling of the electroencephalogram in the auditory cortex in schizophrenia," *Biological Psychiatry: Cognitive Neuroscience and Neuroimaging*, vol. 3, pp. 69–76, Jan 2018.
- [29] N. Murphy, N. Ramakrishnan, C. P. Walker, N. R. Polizzotto, and R. Y. Cho, "Intact auditory cortical cross-frequency coupling in early and chronic schizophrenia," *Frontiers in Psychiatry*, vol. Volume 11 - 2020, 2020.
- [30] D. D. Sacks, P. E. Schwenn, L. T. McLoughlin, J. Lagopoulos, and D. F. Hermens, "Phase-amplitude coupling, mental health and cognition: Implications for adolescence," *Frontiers in Human Neuroscience*, vol. Volume 15 - 2021, 2021.
- [31] B. Yakubov, S. Das, R. Zomorodi, D. M. Blumberger, P. G. Enticott, M. Kirkovski, T. K. Rajji, and P. Desarkar, "Cross-frequency coupling in psychiatric disorders: A systematic review," *Neuroscience & Biobehavioral Reviews*, vol. 138, p. 104690, 2022.
- [32] M. De Pieri, M. Sabe, V. Rochas, G. Poglia, J. Bartolomei, M. Kirschner, and S. Kaiser, "Resting-state eeg and meg gamma frequencies in schizophrenia: a systematic review and exploratory power-spectrum meta-analysis," *Schizophrenia*, vol. 11, p. 48, Mar 2025.
- [33] H. Wang, X. Shi, C. Wang, Y. Qi, M. Gao, and Y. Zhao, "Cross-frequency coupling between low frequency and gamma oscillations altered in cognitive biotype of depression," *Frontiers in Psychiatry*, vol. Volume 16 - 2025, 2025.
- [34] P. Lakatos, G. Karmos, A. D. Mehta, I. Ulbert, and C. E. Schroeder, "Entrainment of neuronal oscillations as a mechanism of attentional selection," *Science*, vol. 320, no. 5872, pp. 110–113, 2008.
- [35] N. Axmacher, M. M. Henseler, O. Jensen, I. Weinreich, C. E. Elger, and J. Fell, "Cross-frequency coupling supports multi-item working memory in the human hippocampus," *Proceedings of the National Academy of Sciences*, vol. 107, no. 7, pp. 3228–3233, 2010.
- [36] T. Yanagisawa, O. Yamashita, M. Hirata, H. Kishima, Y. Saitoh, T. Goto, T. Yoshimine, and Y. Kamitani, "Regulation of motor representation by phase-amplitude coupling in the sensorimotor cortex," *Journal of Neuroscience*, vol. 32, no. 44, pp. 15467–15475, 2012.
- [37] F. Roux and P. J. Uhlhaas, "Working memory and neural oscillations: alpha-gamma versus theta-gamma codes for distinct wm information?," *Trends in Cognitive Sciences*, vol. 18, no. 1, pp. 16–25, 2014.
- [38] R. A. Seymour, G. Rippon, and K. Kessler, "The detection of phase amplitude coupling during sensory processing," *Frontiers in Neuroscience*, vol. Volume 11 - 2017, 2017.
- [39] R. V. Chacko, B. Kim, S. W. Jung, A. L. Daitch, J. L. Roland, N. V. Metcalf, M. Corbetta, G. L. Shulman, and E. C. Leuthardt, "Distinct phase-amplitude couplings distinguish cognitive processes in human attention," *NeuroImage*, vol. 175, pp. 111–121, 2018.
- [40] I. C. Fiebelkorn and S. Kastner, "A rhythmic theory of attention," *Trends in Cognitive Sciences*, vol. 23, no. 2, pp. 87–101, 2019.
- [41] K. Dong, D. Zhang, Q. Wei, G. Wang, F. Huang, X. Chen, K. G. Muhammad, Y. Sun, and J. Liu, "Intrinsic phase-amplitude coupling on multiple spatial scales during the loss and recovery of consciousness," *Computers in Biology and Medicine*, vol. 147, p. 105687, 2022.
- [42] M. Esghaei, S. Treue, and T. R. Vidyasagar, "Dynamic coupling of oscillatory neural activity and its roles in visual attention," *Trends in Neurosciences*, vol. 45, no. 4, pp. 323–335, 2022.
- [43] A. Mockevičius and I. Griškova-Bulanova, "Phase-amplitude coupling during auditory steady-state stimulation: a methodological review," *Reviews in the Neurosciences*, vol. 36, no. 6, pp. 577–586, 2025.
- [44] A. B. L. Tort, R. Komorowski, H. Eichenbaum, and N. Kopell, "Measuring phase-amplitude coupling between neuronal oscillations of different frequencies," *Journal of Neurophysiology*, vol. 104, no. 2, pp. 1195–1210, 2010.
- [45] R. T. Canolty, E. Edwards, S. S. Dalal, M. Soltani, S. S. Nagarajan, H. E. Kirsch, M. S. Berger, N. M. Barbaro, and R. T. Knight, "High gamma power is phase-locked to theta oscillations in human neocortex," *Science*, vol. 313, no. 5793, pp. 1626–1628, 2006.
- [46] W. Penny, E. Duzel, K. Miller, and J. Ojemann, "Testing for nested oscillation," *Journal of Neuroscience Methods*, vol. 174, no. 1, pp. 50–61, 2008.
- [47] T. E. Özkurt, M. Butz, M. Homburger, S. Elben, J. Vesper, L. Wojtecki, and A. Schnitzler, "High frequency oscillations in the subthalamic nucleus: A neurophysiological marker of the motor state in parkinson's disease," *Experimental Neurology*, vol. 229, no. 2, pp. 324–331, 2011.
- [48] M. Kramer and U. Eden, "Assessment of cross-frequency coupling with confidence using generalized linear models," *Journal of Neuroscience Methods*, vol. 220, no. 1, pp. 64–74, 2013.
- [49] B. van Wijk, A. Jha, W. Penny, and V. Litvak, "Parametric estimation of cross-frequency coupling," *Jour-*

- nal of Neuroscience Methods*, vol. 243, pp. 94–102, 2015.
- [50] G. J. Jurkiewicz, M. J. Hunt, and J. Żygierewicz, “Addressing pitfalls in phase-amplitude coupling analysis with an extended modulation index toolbox,” *Neuroinformatics*, vol. 19, pp. 319–345, Apr 2021.
- [51] M. A. Kramer, A. B. Tort, and N. J. Kopell, “Sharp edge artifacts and spurious coupling in eeg frequency comodulation measures,” *Journal of Neuroscience Methods*, vol. 170, no. 2, pp. 352–357, 2008.
- [52] D. Dvorak and A. A. Fenton, “Toward a proper estimation of phase–amplitude coupling in neural oscillations,” *Journal of Neuroscience Methods*, vol. 225, pp. 42–56, 2014.
- [53] J. Aru, J. Aru, V. Priesemann, M. Wibral, L. Lana, G. Pipa, W. Singer, and R. Vicente, “Untangling cross-frequency coupling in neuroscience,” *Current Opinion in Neurobiology*, vol. 31, pp. 51–61, 2015. SI: Brain rhythms and dynamic coordination.
- [54] E. M. Gerber, B. Sadeh, A. Ward, R. T. Knight, and L. Y. Deouell, “Non-sinusoidal activity can produce cross-frequency coupling in cortical signals in the absence of functional interaction between neural sources,” *PLOS ONE*, vol. 11, pp. 1–19, 12 2016.
- [55] O. Jensen, E. Spaak, and H. Park, “Discriminating valid from spurious indices of phase-amplitude coupling,” *eNeuro*, vol. 3, no. 6, 2016.
- [56] D. Dellavale, O. M. Velarde, G. Mato, and E. Urdapilleta, “Complex interplay between spectral harmonicity and different types of cross-frequency couplings in nonlinear oscillators and biologically plausible neural network models,” *Phys. Rev. E*, vol. 102, p. 062401, Dec 2020.
- [57] J. Giehl, N. Noury, and M. Siegel, “Dissociating harmonic and non-harmonic phase-amplitude coupling in the human brain,” *NeuroImage*, vol. 227, p. 117648, 2021.
- [58] A. C. Onslow, R. Bogacz, and M. W. Jones, “Quantifying phase–amplitude coupling in neuronal network oscillations,” *Progress in Biophysics and Molecular Biology*, vol. 105, no. 1, pp. 49–57, 2011. BrainModes: The role of neuronal oscillations in health and disease.
- [59] K. Hasselmann, W. Munk, and G. J. MacDonald, “Bispectra of ocean waves,” in *Symposium on time series analysis* (M. Rodenblatt, ed.), pp. 125–139, Brown University, John Wiley, New York, 1963.
- [60] J. C. Sigl and N. G. Chamoun, “An introduction to bispectral analysis for the electroencephalogram,” *Journal of Clinical Monitoring*, vol. 10, pp. 392–404, Nov 1994.
- [61] H. Witte, B. Schack, M. Helbig, P. Putsche, C. Schein, K. Schmidt, and M. Specht, “Quantification of transient quadratic phase couplings within eeg burst patterns in sedated patients during electroencephalic burst-suppression period,” *Journal of Physiology-Paris*, vol. 94, no. 5, pp. 427–434, 2000.
- [62] A. Hyafil, “Misidentifications of specific forms of cross-frequency coupling: three warnings,” *Frontiers in Neuroscience*, vol. 9, 2015.
- [63] Y. Yang, T. Solis-Escalante, J. Yao, A. Daffertshofer, A. C. Schouten, and F. C. T. van der Helm, “A general approach for quantifying nonlinear connectivity in the nervous system based on phase coupling,” *International Journal of Neural Systems*, vol. 26, no. 01, p. 1550031, 2016.
- [64] C. K. Kovach, H. Oya, and H. Kawasaki, “The bispectrum and its relationship to phase-amplitude coupling,” *NeuroImage*, vol. 173, pp. 518–539, 2018.
- [65] O. M. Velarde, E. Urdapilleta, G. Mato, and D. Dellavale, “Bifurcation structure determines different phase-amplitude coupling patterns in the activity of biologically plausible neural networks,” *NeuroImage*, vol. 202, p. 116031, 2019.
- [66] S. Elgar and R. Guza, “Statistics of bicoherence,” *IEEE Transactions on Acoustics, Speech, and Signal Processing*, vol. 36, no. 10, pp. 1667–1668, 1988.
- [67] K. L. Siu, J. M. Ahn, K. Ju, M. Lee, K. Shin, and K. H. Chon, “Statistical approach to quantify the presence of phase coupling using the bispectrum,” *IEEE Transactions on Biomedical Engineering*, vol. 55, no. 5, pp. 1512–1520, 2008.
- [68] S. Chen and S. A. Billings, “Representations of nonlinear systems: the narimax model,” *International Journal of Control*, vol. 49, no. 3, pp. 1013–1032, 1989.
- [69] S. CHEN, S. A. BILLINGS, and W. LUO, “Orthogonal least squares methods and their application to nonlinear system identification,” *International Journal of Control*, vol. 50, no. 5, pp. 1873–1896, 1989.
- [70] S. B. Yuzhu Guo, L.Z. Guo and H.-L. Wei, “An iterative orthogonal forward regression algorithm,” *International Journal of Systems Science*, vol. 46, no. 5, pp. 776–789, 2015.
- [71] S. Billings, *Nonlinear System Identification: NARMAX Methods In The Time, Frequency, And Spatio-Temporal Domains*, vol. 13. Chichester, UK: John Wiley & Sons, Ltd, 2013.
- [72] N. Chiras, C. Evans, and D. Rees, “Global Nonlinear Modeling of Gas Turbine Dynamics Using NARMAX Structures,” *Journal of Engineering for Gas Turbines and Power*, vol. 124, pp. 817–826, 09 2002.
- [73] K. Wang, J. Zhang, A. J. Croxford, and Y. Yang, “Nonlinear autoregressive exogenous method for structural health monitoring using ultrasonic guided waves,” in *Structural Health Monitoring/ Management (SHM) in Aerospace Structures* (F.-G. Yuan, ed.), Woodhead Publishing Series in Composites Science and Engineering, pp. 427–452, Woodhead Publishing, 2024.
- [74] N. M. Zainol, N. S. Damanhuri, N. A. Othman, Y. S. Chiew, M. B. M. Nor, Z. Muhammad, and J. G. Chase, “Estimating the incidence of spontaneous breathing effort of mechanically ventilated patients using a nonlinear auto regressive (narx) model,” *Computer Methods and Programs in Biomedicine*, vol. 220, p. 106835, 2022.
- [75] D. Ritzberger and S. Jakubek, “Nonlinear data-driven identification of polymer electrolyte membrane fuel cells for diagnostic purposes: A volterra series approach,” *Journal of Power Sources*, vol. 361, pp. 144–152, 2017.
- [76] Y. Gao, C. Yu, Y.-P. Zhu, and Z. Luo, “A narx model-based condition monitoring method for rotor systems,”

- Sensors*, vol. 23, no. 15, 2023.
- [77] F. He, P. Sarrigiannis, S. Billings, H. Wei, J. Rowe, C. Romanowski, N. Hoggard, M. Hadjivassiliou, D. Rao, R. Grünwald, A. Khan, and J. Yianni, “Non-linear interactions in the thalamocortical loop in essential tremor: A model-based frequency domain analysis,” *Neuroscience*, vol. 324, pp. 377–389, 2016.
- [78] F. He and Y. Yang, “Nonlinear system identification of neural systems from neurophysiological signals,” *Neuroscience*, vol. 458, pp. 213–228, 2021.
- [79] Z. Liu, Z.-Q. Lang, Y. Gui, Y.-P. Zhu, and H. Laalej, “Digital twin-based anomaly detection for real-time tool condition monitoring in machining,” *Journal of Manufacturing Systems*, vol. 75, pp. 163–173, 2024.
- [80] B. Voloh, T. A. Valiante, S. Everling, and T. Womelsdorf, “Theta-gamma coordination between anterior cingulate and prefrontal cortex indexes correct attention shifts,” *Proceedings of the National Academy of Sciences*, vol. 112, no. 27, pp. 8457–8462, 2015.
- [81] A. Bragin, G. Jando, Z. Nadasdy, J. Hetke, K. Wise, and G. Buzsáki, “Gamma (40-100 Hz) oscillation in the hippocampus of the behaving rat,” *Journal of Neuroscience*, vol. 15, no. 1, pp. 47–60, 1995.
- [82] A. C. E. Onslow, M. W. Jones, and R. Bogacz, “A canonical circuit for generating phase-amplitude coupling,” *PLOS ONE*, vol. 9, pp. 1–15, 08 2014.
- [83] T. Dupré la Tour, L. Tallot, L. Grabot, V. Doyère, V. van Wassenhove, Y. Grenier, and A. Gramfort, “Non-linear auto-regressive models for cross-frequency coupling in neural time series,” *PLOS Computational Biology*, vol. 13, pp. 1–32, 12 2017.
- [84] G. Prendergast, S. R. Johnson, and G. G. R. Green, “Temporal dynamics of sinusoidal and non-sinusoidal amplitude modulation,” *European Journal of Neuroscience*, vol. 32, no. 9, pp. 1599–1607, 2010.
- [85] S. R. Cole and B. Voytek, “Brain oscillations and the importance of waveform shape,” *Trends in Cognitive Sciences*, vol. 21, no. 2, pp. 137–149, 2017.
- [86] M. Breakspear, “Dynamic models of large-scale brain activity,” *Nature Neuroscience*, vol. 20, pp. 340–352, Mar 2017.
- [87] Y. Qin, T. Menara, D. S. Bassett, and F. Pasqualetti, “Phase-amplitude coupling in neuronal oscillator networks,” *Phys. Rev. Res.*, vol. 3, p. 023218, Jun 2021.
- [88] M. K. Nandi, M. Valla, and M. di Volo, “Bursting gamma oscillations in neural mass models,” *Frontiers in Computational Neuroscience*, vol. Volume 18 - 2024, 2024.
- [89] H. R. Wilson and J. D. Cowan, “Excitatory and inhibitory interactions in localized populations of model neurons,” *Biophysical Journal*, vol. 12, no. 1, pp. 1–24, 1972.
- [90] H. R. Wilson and J. D. Cowan, “A mathematical theory of the functional dynamics of cortical and thalamic nervous tissue,” *Kybernetik*, vol. 13, pp. 55–80, Sep 1973.
- [91] Z. P. Kilpatrick, *Wilson-Cowan Model*, pp. 1–5. New York, NY: Springer New York, 2013.
- [92] R. C. Sotero, “Topology, cross-frequency, and same-frequency band interactions shape the generation of phase-amplitude coupling in a neural mass model of a cortical column,” *PLOS Computational Biology*, vol. 12, pp. 1–29, 11 2016.
- [93] L. L. Colgin, T. Denninger, M. Fyhn, T. Hafting, T. Bonnevie, O. Jensen, M.-B. Moser, and E. I. Moser, “Frequency of gamma oscillations routes flow of information in the hippocampus,” *Nature*, vol. 462, pp. 353–357, Nov 2009.
- [94] M. J. Hülsemann, E. Naumann, and B. Rasch, “Quantification of phase-amplitude coupling in neuronal oscillations: Comparison of phase-locking value, mean vector length, modulation index, and generalized-linear-modeling-cross-frequency-coupling,” *Frontiers in Neuroscience*, vol. 13, 2019.
- [95] S. Samiee and S. Baillet, “Time-resolved phase-amplitude coupling in neural oscillations,” *NeuroImage*, vol. 159, pp. 270–279, 2017.
- [96] M. A. Belluscio, K. Mizuseki, R. Schmidt, R. Kempster, and G. Buzsáki, “Cross-frequency phase-phase coupling between theta and gamma oscillations in the hippocampus,” *Journal of Neuroscience*, vol. 32, no. 2, pp. 423–435, 2012.
- [97] Z.-Q. Lang and S. A. Billings, “Output frequency characteristics of nonlinear systems,” *International Journal of Control*, vol. 64, no. 6, pp. 1049–1067, 1996.
- [98] Z.-Q. Lang and S. A. Billings, “Output frequencies of nonlinear systems,” *International Journal of Control*, vol. 67, no. 5, pp. 713–730, 1997.
- [99] Z. Q. L. * and S. A. Billings, “Energy transfer properties of non-linear systems in the frequency domain,” *International Journal of Control*, vol. 78, no. 5, pp. 345–362, 2005.
- [100] C. S. Herrmann, “Human eeg responses to 1–100Hz flicker: resonance phenomena in visual cortex and their potential correlation to cognitive phenomena,” *Experimental Brain Research*, vol. 137, pp. 346–353, Apr 2001.
- [101] S. Tobimatsu, Y. M. Zhang, and M. Kato, “Steady-state vibration somatosensory evoked potentials: physiological characteristics and tuning function,” *Clinical Neurophysiology*, vol. 110, no. 11, pp. 1953–1958, 1999.
- [102] C. S. Herrmann, M. M. Murray, S. Ionta, A. Hutt, and J. Lefebvre, “Shaping intrinsic neural oscillations with periodic stimulation,” *Journal of Neuroscience*, vol. 36, no. 19, pp. 5328–5337, 2016.
- [103] X. Chen, Z. Chen, S. Gao, and X. Gao, “Brain-computer interface based on intermodulation frequency,” *Journal of Neural Engineering*, vol. 10, p. 066009, oct 2013.
- [104] A. S. Giani, E. Ortiz, P. Belardinelli, M. Kleiner, H. Preissl, and U. Noppeney, “Steady-state responses in meg demonstrate information integration within but not across the auditory and visual senses,” *NeuroImage*, vol. 60, no. 2, pp. 1478–1489, 2012.
- [105] N. Gordon, J. Hohwy, M. J. Davidson, J. J. van Boxtel, and N. Tsuchiya, “From intermodulation components to visual perception and cognition—a review,” *NeuroImage*, vol. 199, pp. 480–494, 2019.
- [106] C. E. Luff, R. Peach, E.-J. Mallas, E. Rhodes, F. Laumann, E. S. Boyden, D. J. Sharp, M. Barahona, and N. Grossman, “The neuron mixer and its impact on

- human brain dynamics,” *Cell Reports*, vol. 43, no. 6, p. 114274, 2024.
- [107] L. Ljung, “Perspectives on system identification,” *Annual Reviews in Control*, vol. 34, no. 1, pp. 1–12, 2010.
- [108] R. Gunawardena, Z.-Q. Lang, and F. He, “Nonsysid: A nonlinear system identification package with improved model term selection for narmax models,” 2024.
- [109] R. Gunawardena, Z.-Q. Lang, and F. He, “GitHub - NonSysID: A MatLab package for System Identification using linear and nonlinear auto-regressive models—(N)AR, (N)ARX and (N)ARMAX models.” <https://github.com/raj-gun/NonSysID>, 2024. [Accessed 07-08-2025].
- [110] B. P. Lathi and R. A. Green, *Linear Systems and Signals*, ch. B.2, pp. 18–20. Oxford, UK: Oxford University Press, 3 ed., 2017.
- [111] E. M. A. M. Mendes and S. A. Billings, “On over-parametrization of nonlinear discrete systems,” *International Journal of Bifurcation and Chaos*, vol. 08, no. 03, pp. 535–556, 1998.
- [112] D. Kugiuntzis, “State space reconstruction parameters in the analysis of chaotic time series — the role of the time window length,” *Physica D: Nonlinear Phenomena*, vol. 95, no. 1, pp. 13–28, 1996.
- [113] E. Tan, S. Algar, D. Corrêa, M. Small, T. Stemler, and D. Walker, “Selecting embedding delays: An overview of embedding techniques and a new method using persistent homology,” *Chaos: An Interdisciplinary Journal of Nonlinear Science*, vol. 33, p. 032101, 03 2023.
- [114] L. A. AGUIRRE and S. A. BILLINGS, “Improved structure selection for nonlinear models based on term clustering,” *International Journal of Control*, vol. 62, no. 3, pp. 569–587, 1995.
- [115] L. A. AGUIRRE and E. M. A. M. MENDES, “Global nonlinear polynomial models: Structure, term clusters and fixed points,” *International Journal of Bifurcation and Chaos*, vol. 06, no. 02, pp. 279–294, 1996.
- [116] L. A. Aguirre, G. G. Rodrigues, and E. M. A. M. Mendes, “Nonlinear identification and cluster analysis of chaotic attractors from a real implementation of chua’s circuit,” *International Journal of Bifurcation and Chaos*, vol. 07, no. 06, pp. 1411–1423, 1997.
- [117] V. Miskovic, K. J. MacDonald, L. J. Rhodes, and K. A. Cote, “Changes in eeg multiscale entropy and power-law frequency scaling during the human sleep cycle,” *Human Brain Mapping*, vol. 40, no. 2, pp. 538–551, 2019.
- [118] B. J. He, “Scale-free brain activity: past, present, and future,” *Trends in Cognitive Sciences*, vol. 18, no. 9, pp. 480–487, 2014.
- [119] K. H. Pettersen, H. Lindén, T. Tetzlaff, and G. T. Einevoll, “Power laws from linear neuronal cable theory: Power spectral densities of the soma potential, soma membrane current and single-neuron contribution to the eeg,” *PLOS Computational Biology*, vol. 10, pp. 1–26, 11 2014.
- [120] Y. Ao, P. Klar, Y. Catal, Y. Wang, and G. Northoff, “Infra-slow scale-free dynamics modulate the connection of neural and behavioral variability during attention,” *Communications Biology*, vol. 8, p. 1057, Jul 2025.
- [121] M. Caiola, A. Devergnas, M. H. Holmes, and T. Wichmann, “Empirical analysis of phase-amplitude coupling approaches,” *PLOS ONE*, vol. 14, pp. 1–18, 07 2019.
- [122] W. Spinelli, L. Piroddi, and M. Lovera, “On the role of pre-filtering in nonlinear system identification,” *IFAC Proceedings Volumes*, vol. 38, no. 1, pp. 791–796, 2005. 16th IFAC World Congress.
- [123] S. Anderson and V. Kadiramanathan, “Modelling and identification of non-linear deterministic systems in the delta-domain,” *Automatica*, vol. 43, no. 11, pp. 1859–1868, 2007.
- [124] R. Scheffer-Teixeira, H. Belchior, F. V. Caixeta, B. C. Souza, S. Ribeiro, and A. B. L. Tort, “Theta phase modulates multiple layer-specific oscillations in the ca1 region,” *Cerebral Cortex*, vol. 22, pp. 2404–2414, 11 2011.
- [125] Tortlab, “GitHub - tortlab/phase-amplitude-coupling: Matlab routines for computing the Modulation Index and Comodulogram, as described in Tort et al., J Neurophysiol 2010 — github.com.” <https://github.com/tortlab/phase-amplitude-coupling>, 2018. [Accessed 06-08-2025].
- [126] D. Lozano-Soldevilla, N. ter Huurne, and R. Oostenveld, “Neuronal oscillations with non-sinusoidal morphology produce spurious phase-to-amplitude coupling and directionality,” *Frontiers in Computational Neuroscience*, vol. Volume 10 - 2016, 2016.
- [127] M. Amiri, J.-M. Lina, F. Pizzo, and J. Gotman, “High frequency oscillations and spikes: Separating real hfos from false oscillations,” *Clinical Neurophysiology*, vol. 127, no. 1, pp. 187–196, 2016.
- [128] M. A. Little, G. Varoquaux, S. Saeb, L. Lonini, A. Jayaraman, D. C. Mohr, and K. P. Kording, “Using and understanding cross-validation strategies. Perspectives on Saeb et. al.,” *GigaScience*, vol. 6, p. gix020, 03 2017.
- [129] M. Stone, “Cross-validators choice and assessment of statistical predictions,” *Journal of the Royal Statistical Society. Series B (Methodological)*, vol. 36, no. 2, pp. 111–147, 1974.
- [130] L. Wang and W. R. Cluett, “Use of press residuals in dynamic system identification,” *Automatica*, vol. 32, no. 5, pp. 781–784, 1996.
- [131] X. Hong, P. Sharkey, and K. Warwick, “Automatic nonlinear predictive model-construction algorithm using forward regression and the press statistic,” *IEEE Proceedings-Control Theory and Applications*, vol. 150, no. 3, pp. 245–254, 2003.
- [132] H.-L. Wei, S. A. Billings, and J. Liu, “Term and variable selection for non-linear system identification,” *International Journal of Control*, vol. 77, no. 1, pp. 86–110, 2004.

Appendix A: A brief on System Identification of nonlinear systems

1. Nonlinear system identification

System identification is a machine learning technique for deriving time-series models that describe the dynamic behaviour of linear and nonlinear systems using experimental input–output data. The resulting dynamic models are typically linear or nonlinear autoregressive with exogenous inputs (ARX or NARX), meaning that the present output is expressed as a function of past input and output values. System identification serves two main objectives:

- Accurately mapping the input(s) to the output(s) of the system, enabling reliable prediction for new, unseen data.
- Faithfully capturing the underlying system dynamics within the model structure.

To meet these objectives, system identification seeks a functional relationship mapping past inputs (input-lagged terms),

$$U = \left\{ u_1(t-1), \dots, u_1(t-n_{b_1}), \right. \\ \left. u_2(t-1), \dots, u_2(t-n_{b_2}) \right\}, \quad (\text{A1})$$

and past outputs (output-lagged terms),

$$Y = \left\{ y(t-1), y(t-2), \dots, y(t-n_a) \right\}, \quad (\text{A2})$$

to the present output in time $y(t)$. Equations (A1) and (A2) are an example of lagged input-output data of a two-input single-output system, where $u_1(t)$ and $u_2(t)$ are two different inputs. n_a is the maximum number of past output time instances (output delays) considered. n_{b_1} and n_{b_2} are the maximum number of past input time instances (input delays) considered for $u_1(t)$ and $u_2(t)$ respectively. These values are related to the Lyapunov exponents of the actual system that is being modelled [111]. The said functional mapping is described by the equation:

$$y(t) = f^{N_p}(Y, U) + \xi(t), \quad (\text{A3})$$

where $f^{N_p}(\cdot)$ is a polynomial function with a maximum polynomial degree $N_p \in \mathbb{Z}^+$. Y and U refer to the input-output lagged data, while $\xi(t)$ represents the error between the predicted output $f(Y, U)$ and the actual output $y(t)$ at time instance t . $\xi(t)$ will contain noise and unmodeled dynamics. In the case of polynomial (N)ARX models, equation (A3) can be expressed as

$$y(t) = \sum_{m=1}^{\mathcal{M}} \theta_m \times \phi_m(t) + \xi(t), \quad (\text{A4})$$

where $m = 1, \dots, \mathcal{M}$, \mathcal{M} being the total number of variables or model terms. θ_m are the model parameters or coefficients and $\phi_m(t)$ are the corresponding model terms or variables. $\phi_m(t)$ are n^{th} -order monomials of the polynomial NARX model $f^{N_p}(\cdot)$, where $n = 1, \dots, N_p$ is the degree of the monomial. $\phi_m(t)$ is composed of past output and input time instances from Y and U respectively. An example of a polynomial NARX model can be

$$y(t) = \theta_1 y(t-1) + \theta_2 u_1(t-2) + \\ \theta_3 y(t-2)^2 u_2(t-1)^3 + \xi(t). \quad (\text{A5})$$

In the above example, $\phi_1(t) = y(t-1)$ and $\phi_2(t) = u_1(t-2)$ have a degree of 1 and are linear terms (degree or order of monomial is 1) of the model. While $\phi_3(t) = y(t-2)^2 u_2(t-1)^3$ is a nonlinear term with a degree of 5 (degree or order of monomial is 5). The NARX model shown in equation (A5) has a polynomial degree $N_p = 5$ (highest degree of any monomial). Given that the total number of time samples available is L , where $t = 1, \dots, L$. Equation (A4) can be represented in matrix form as

$$\mathbf{Y} = \mathbf{\Phi}\mathbf{\Theta} + \mathbf{\Xi}, \quad (\text{A6})$$

where $\mathbf{Y} = [y(1), \dots, y(L)]^T$ is the vector containing the output samples $y(t)$. $\mathbf{\Phi} = [\bar{\phi}_1, \dots, \bar{\phi}_{\mathcal{M}}]$, where $\bar{\phi}_m = [\phi_m(1), \dots, \phi_m(L)]^T$ is the vector containing all time samples of the model variable $\phi_m(t)$. $\mathbf{\Theta} = [\theta_1, \dots, \theta_{\mathcal{M}}]^T$ is the parameter vector and $\mathbf{\Xi} = [\xi(1), \dots, \xi(L)]$ is the vector containing all the error terms $\xi(t)$.

The main concern in learning a NARX model is to identify the polynomial structure of the model, i.e. from a set of candidate model terms (monomials), D , which terms should be included in the model. For example, a possible set of candidate terms could be

$$D = \left\{ y(t-1), y(t-2), u_1(t-1), u_1(t-2), \right. \\ \left. y(t-1)u_1(t-2), y(t-2)u_2(t-1)^3, \right. \\ \left. y(t-2)^2 u_1(t-1), y(t-2)^2 u_2(t-1)^3 \right\}, \quad (\text{A7})$$

from which a NARX model structure such as in equation (A5) could be identified. Once the model structure is identified, the parameters of the model need to be estimated. Given the input-output data of a dynamic system that is to be modelled, the model structure has to be determined so that a parsimonious model is obtained. This is important especially in the nonlinear case so that the model identified, because of the unnecessary model terms, does not contain any dynamics that should not be there [111]. In addition, a model should generalise well to data (validation) that is not

used during the learning or training process (model identification process). This is known as obtaining a bias-variance compromise and is achieved through an appropriate cross-validation strategy [128, 129]. For this purpose, we use the iFRO algorithm [70] for model term selection with the prediction sum of squares statistic (PRESS-statistic) [130, 131] as the term selection criterion.

As mentioned in Section III C, in this study, input-only second-order NARX models are used for the canonical approximation of PAC. This means the maximum polynomial order considered is $N_p = 2$ and only past input-lagged terms (equation (A1)) are used to identify the NARX model.

2. System identification algorithm

The iFRO algorithm [70] is capable of evaluating the contribution of each candidate model term to the output, independently of the influence exerted by other terms. This property enables efficient term selection within a forward-selection framework, in which model terms are incorporated sequentially according to a specified selection criterion, thereby facilitating the construction of a globally optimal parsimonious model [70]. When combined with the PRESS-statistic [130, 131], iFRO preferentially selects model terms that minimise the predicted leave-one-out cross-validation error in a forward-selection manner, thus maximising generalisation performance without the need for a dedicated validation dataset [130, 131]. In addition, the final identified model must be stable in simulation to ensure reliable dynamical reproduction.

NonSysID [108, 109] is an open-source software framework for system identification employing the NARX model structure, integrating iFRO with PRESS-statistic-based term selection. Moreover, *NonSysID* incorporates the procedures outlined in [132], which expedite the identification process by initially estimating an ARX model and subsequently using its terms to construct candidate nonlinear terms for NARX model identification. This strategy is theoretically appropriate and accelerates the canonical approximation process (Section III C), as elaborated below.

As detailed in Section III A and further examined in Section II A, the slow and fast oscillations, $x(t)$ and $h(t)$ respectively, interact nonlinearly to generate the amplitude modulation $y(t)$ (see equations (2) and (3)). In accordance with [132], an initial ARX model can be identified to capture the independent dynamics of $x(t)$ and $h(t)$. The identified terms are then multiplicatively combined to form the 2nd-order candidate nonlinear terms, which serve as the basis for identifying a NARX model that encapsulates the nonlinear dynamics governing $y(t)$ (Fig. 10). Owing to these methodolog-

ical features, the *NonSysID* package [108, 109] is particularly well-suited for the canonical approximation of PAC via system identification.

Appendix B: Taylor approximations of complex PAC-generating mechanisms

This section shows how complex PAC-generating mechanisms, such as non-sinusoidal amplitude modulation (equation (3)) and the NMM (equation (5))—implicitly contain the basic PAC model (equation (2)). This is demonstrated by applying Taylor approximations to the governing equations of these complex mechanisms.

1. Taylor approximation of equation (3)

Using a Taylor expansion of the shifted and scaled sigmoid function about $x(t) = 0$, equation (3) can be written as

$$y(t) \approx \left(1 - q_0 - q_1 x(t) - q_2 x^2(t) - \dots\right) h(t) \quad (\text{B1})$$

where

$$\begin{aligned} q_0 &= \frac{1}{1 + e^{\alpha c}} \\ q_1 &= \alpha \frac{e^{\alpha c}}{(1 + e^{\alpha c})^2} \\ q_2 &= \alpha^2 \frac{e^{\alpha c}(e^{\alpha c} - 1)}{2(1 + e^{\alpha c})^3} \end{aligned} \quad (\text{B2})$$

Therefore, considering a first-order Taylor series approximation, equation (3) can be reduced to a form similar to equation (2), as shown below

$$y(t) \approx \left((1 - q_0) - q_1 x(t)\right) h(t) \quad (\text{B3})$$

Therefore, substituting this into equation (1), the first-order Taylor approximation of PAC with non-sinusoidal amplitude modulation can be expressed as

$$z(t) = x(t) + \left((1 - q_0) - q_1 x(t)\right) h(t), \quad (\text{B4})$$

which has a similar form to the most basic PAC model shown in equations (1) and (2).

2. Taylor approximation of equation (5)

A Taylor expansion of the shifted and scaled sigmoid function, $f(z)$, in equation (7), about $z = 0$, is given as

$$f(z) \approx c_0 + c_1 z + c_2 z^2 + c_3 z^3 + \dots \quad (\text{B5})$$

where

$$\begin{aligned}
c_0 &= \frac{1}{1 + e^b} \\
c_1 &= b c_0(1 - c_0) \\
c_2 &= \frac{b^2}{2} c_0(1 - c_0)(1 - 2c_0) \\
c_3 &= \frac{b^3}{6} c_0(1 - c_0)(1 - 6c_0 + 6(c_0)^2).
\end{aligned} \tag{B6}$$

Using a second-order Taylor approximation, equation (5) can be written as

$$\tau_E \dot{E}(t) \approx -E(t) + c_0 + c_1 z_E(t) + c_2 z_E^2(t), \tag{B7}$$

where $z_E(t) = x_E(t) + w_{EE}E(t) - w_{IE}I(t)$. Denoting $h(t) = w_{EE}E(t) - w_{IE}I(t)$, equation (B7) can be expressed as

$$\begin{aligned}
\tau_E \dot{E}(t) &\approx -E(t) + c_0 + c_1 x_E(t) + \left(c_1 + 2c_2 x_E(t)\right) h(t) \\
&\quad + c_2 \left(x_E^2(t) + h^2(t)\right)
\end{aligned} \tag{B8}$$

The corresponding terms from equation (B8),

$$z(t) = c_1 x_E(t) + \left(c_1 + 2c_2 x_E(t)\right) h(t) \tag{B9}$$

has a similar form to the most basic PAC model shown in equations (1) and (2).

The NMM defined by equations (5)–(7) (as illustrated in Fig. 1) can be decomposed (using the Taylor approximation in (B8)) to separate the slow oscillation dynamics, $x(t)$, from the amplitude-modulated fast oscillation dynamics, $y(t)$, such that

$$x(t) \approx c_1 x_E + c_2 x_E^2(t) + \dots \tag{B10}$$

and

$$y(t) \approx c_1 h(t) + c_2 h^2(t) + 2c_2 x_E(t) h(t) + \dots \tag{B11}$$

The above decomposition becomes more accurate when higher-order terms from the Taylor expansion of $f(z)$ are included.

Appendix C: Supplementary figures

This appendix includes all the supplementary figures used in this paper.

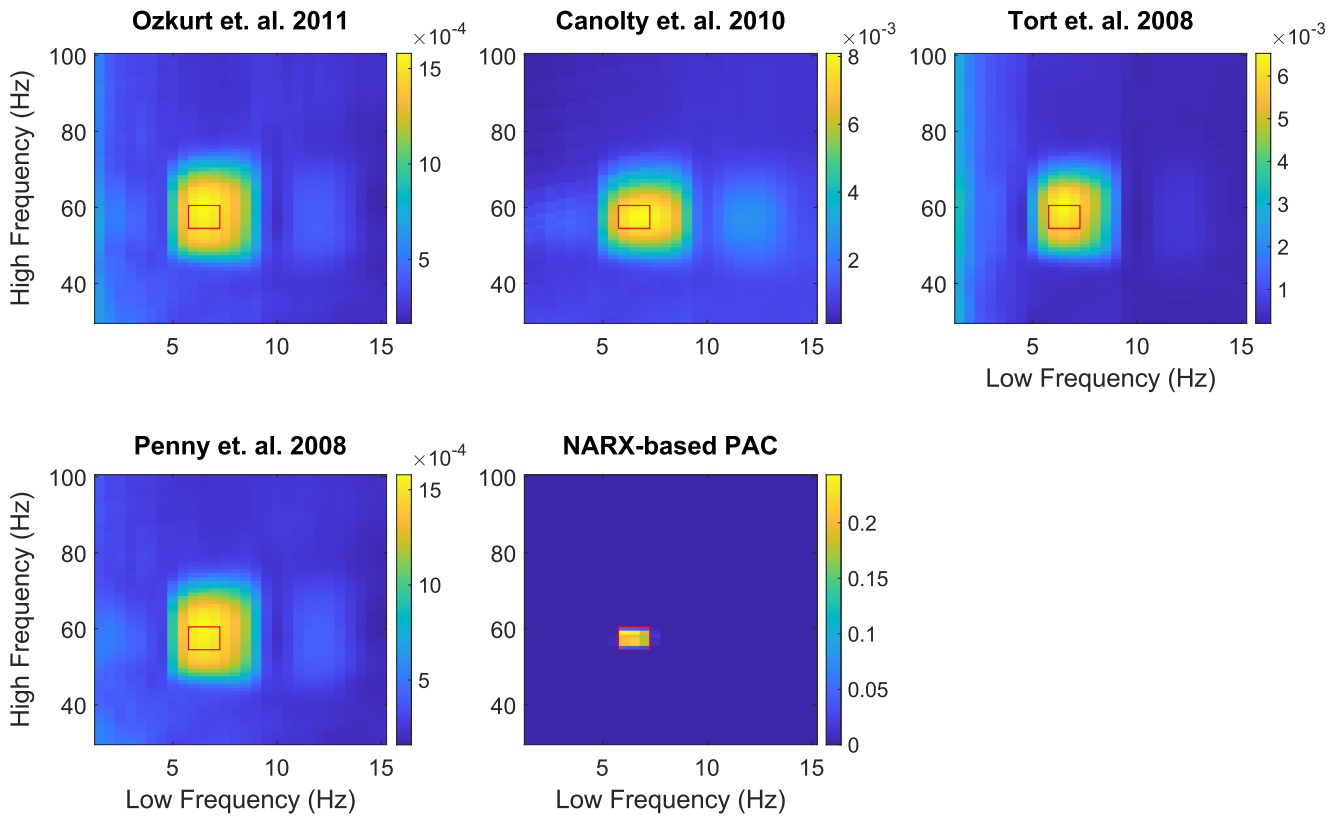


Figure 19. **Average of 100 samples: Non-stationary slow oscillation (6–7 Hz) coupled to a non-stationary fast oscillation (55–60 Hz).** This figure compares the average comodulograms obtained from 100 PAC signal realisations with identical coupling dynamics. Each PAC signal was constructed using a different pink-noise sample (Fig. 11). The red box marks the region of the comodulograms where PAC is present. Comparisons with alternative methods demonstrate the repeatability and specificity of the proposed NARX-PAC method.

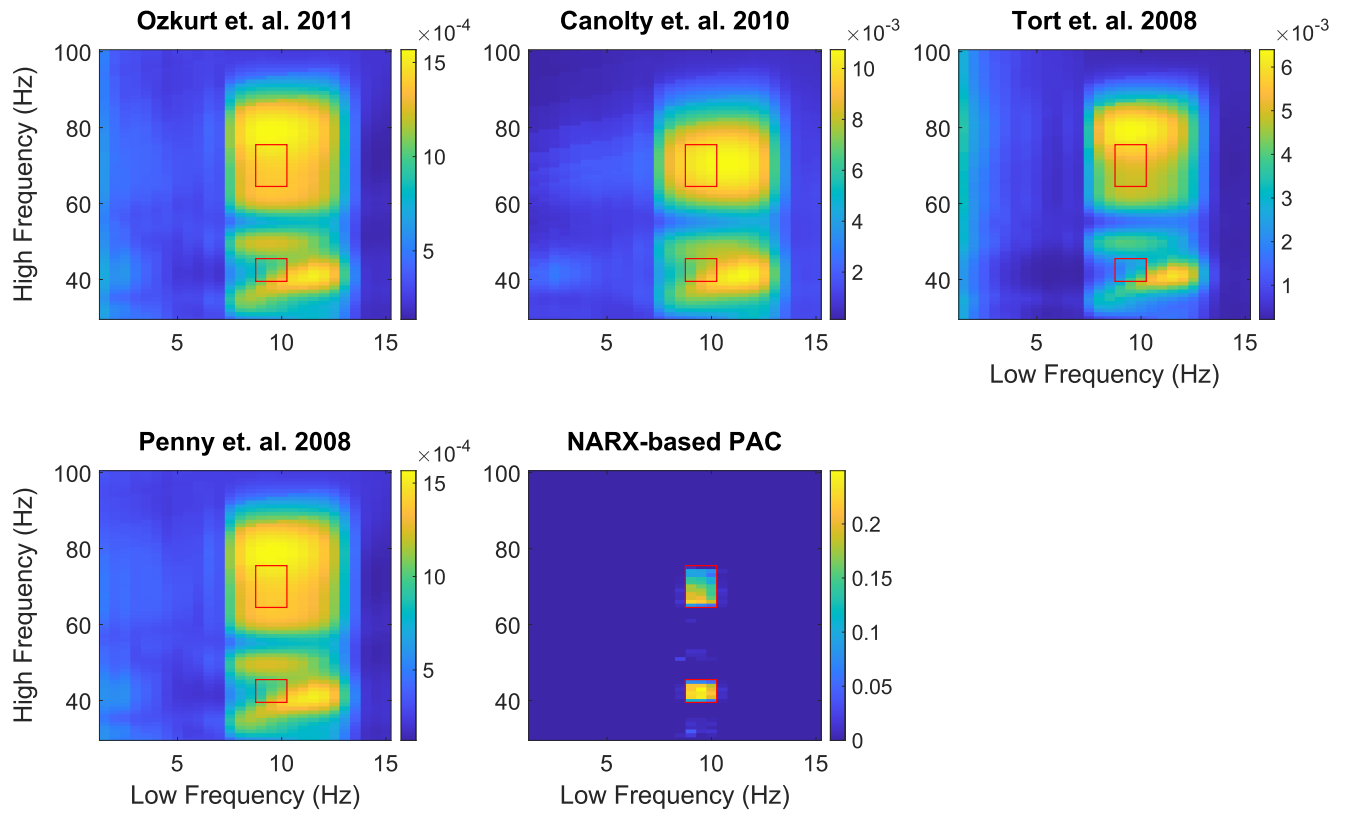


Figure 20. **Average of 100 samples: Non-stationary slow oscillation (9–10 Hz) coupled to two non-stationary fast oscillations (40–45 Hz and 65–75 Hz).** This figure compares the average comodulograms obtained from 100 PAC signal realisations with identical coupling dynamics. Each PAC signal was constructed using a different pink-noise sample (Fig. 11). The red boxes mark the regions of the comodulograms where PAC is present. Comparisons with alternative methods demonstrate the repeatability and specificity of the proposed NARX-PAC method.